

Millimeter and Submillimeter Excess Emission in M33 revealed by Planck and LABOCA.

I. Hermelo¹, M. Relaño^{2,3}, U. Lisenfeld^{2,3}, S. Verley^{2,3}, C. Kramer¹, T. Ruiz-Lara^{2,3}, M. Boquien⁴, E. M. Xilouris⁵, and M. Albrecht⁶

¹ Instituto Radioastronomía Milimétrica (IRAM), Av. Divina Pastora 7, Núcleo Central, 18012, Granada, Spain
e-mail: hermelo@iram.es

² Departamento de Física Teórica y del Cosmos, Universidad de Granada, 18071, Granada, Spain

³ Instituto Universitario Carlos I de Física Teórica y Computacional, Universidad de Granada, 18071 Granada, Spain

⁴ Institute of Astronomy, University of Cambridge, Madingley Road, Cambridge CB3 0HA, UK

⁵ Institute for Astronomy, Astrophysics, Space Applications & Remote Sensing, National Observatory of Athens, P. Penteli, 15236, Athens, Greece

⁶ Argelander-Institut für Astronomie, Universität Bonn, Germany

Preprint online version: March 1, 2022

ABSTRACT

Context. Previous studies have shown the existence of an excess of emission at submillimeter (submm) and millimeter (mm) wavelengths in the spectral energy distribution (SED) of many low-metallicity galaxies. The so-called “submm excess”, whose origin remains unknown, challenges our understanding of the dust properties in low-metallicity environments.

Aims. The goal of the present study is to model separately the emission from the star forming (SF) component and the emission from the diffuse interstellar medium (ISM) in the nearby spiral galaxy M33, in order to check if both components can be well fitted using radiation transfer models or if there is an excess of submm emission associated to any or both of them.

Methods. We decomposed the observed SED of M33 into its SF and diffuse components. Mid-infrared (MIR) and far-infrared (FIR) fluxes were extracted from *Spitzer* and *Herschel* data. At submm and mm wavelengths, we used ground-based observations from *APEX* to measure the emission from the SF component and data from the *Planck* space telescope to estimate the diffuse emission. Both components were separately fitted using radiation transfer models based on standard dust properties (i.e. emissivity index $\beta=2$) and a realistic geometry. The large amount of previous studies helped us to estimate the thermal radio emission and to constrain an important part of the input parameters of the models. Both modeled SEDs were combined to build the global SED of M33. In addition, the radiation field necessary to power the dust emission in our modeling was compared with observations from *GALEX*, *Sloan*, and *Spitzer*.

Results. Our modeling is able to reproduce the observations at MIR and FIR wavelengths, but we found a strong excess of emission at submm and mm wavelengths, where the model expectations severely underestimate the LABOCA and *Planck* fluxes. We also found that the ultraviolet (UV) radiation escaping the galaxy is 70% higher than the model predictions. From the total mass of dust derived from our modeling and the mass of atomic and molecular gas measured with the *VLA* and the IRAM 30 m telescope, we determined a gas-to-dust mass ratio $G_{\text{dust}} \sim 100$, significantly lower than the value expected from the sub-solar metallicity of M33.

Conclusions. We discussed different hypotheses to explain the discrepancies found in our study (i.e., excess of emission at submm and mm wavelengths, deficit of UV attenuation, and abnormally low value of G_{dust}), concluding that different dust properties in M33 is the most plausible explanation.

Key words. dust, extinction – Galaxies: individual: M33 – Galaxies: ISM – Galaxies: star formation – submillimeter: galaxies

1. Introduction

Dust grains are mixed with the gas in all the components and phases of a galaxy, from the ionized gas and the photo-dissociation regions (PDRs) embedded in the star forming (SF) regions, to the diffuse interstellar medium (ISM). Depending on their environment, dust grains are exposed to very different radiation fields and physical conditions. While the interstellar dust within the SF component is immersed in the intense ultraviolet (UV) radiation coming from massive, hot stars, dust grains in the diffuse ISM are more likely illuminated by the radiation field of the old stellar population (Hippenleijn et al. 2003; Verley et al. 2009). These differences not only change the grain heating and the subsequent emission, but also might change the grain properties (e.g., size distribution, chemical composition, ionization

state) and play an important role on the dust evolution (Hippenleijn et al. 2003; Paradis et al. 2011).

Modeling the spectral energy distribution (SED) emitted by the dust grains is a powerful tool to understand the grain properties as well as the interaction between the interstellar dust and the radiation field. One of the most simple approaches to model the dust emission is the modified black body (MBB), where the intensity, S_ν , is expressed as:

$$S_\nu \propto B_\nu(T) \nu^\beta, \quad (1)$$

where $B_\nu(T)$ is the Planck function and β is the dust emissivity index, which in the case of idealized spherical dielectric grains adopts the value $\beta=2$. Although the MBB models are highly degenerated (there is no unique solution for β and T , see Tabatabaei et al. 2014 for a detailed analysis), they have been widely used

to study the dust emission (e.g., Kirkpatrick et al. 2013; Gordon et al. 2014).

More sophisticated models have also been used, from phenomenological models based on realistic dust properties (e.g., Galliano et al. 2011), to fully three-dimensional radiation transfer models (Ercolano et al. 2005). Although the different methodologies applied make the comparison of these studies somehow difficult, many of them have shown that it is not possible to reproduce the SEDs of low-metallicity galaxies due to an excess of observed emission at submillimeter (submm) wavelengths (e.g., Lisenfeld et al. 2002; Galliano et al. 2003, 2005; Bendo et al. 2006; Galametz et al. 2009, 2011; Israel et al. 2010; Bot et al. 2010; Dale et al. 2012; Planck Collaboration 2011).

The origin of this problem, usually known as the *submm excess*, is not clear yet. The existence of a large amount of cold dust could in principle produce the observed shape, but the required dust mass is unreasonably high (e.g., Lisenfeld et al. 2002) and the gas-to-dust mass ratio too low (e.g., Galliano et al. 2011; Galametz et al. 2011; Gordon et al. 2014). Different dust grain properties, and in particular a lower β in the submm have also been suggested (e.g., Lisenfeld et al. 2002; Galliano et al. 2011; Gordon et al. 2014). For example, if hydrogenated amorphous carbon grains were the most probable form of carbonaceous grains in the ISM (instead of graphite), this could significantly flatten the SED in the submm range (Serra Díaz-Cano & Jones 2008; Jones et al. 2013). More exotic explanations have also been proposed, from magnetic nanograins emitting at the microwave and submm wavelengths (Draine & Hensley 2012) to spinning grains (Draine & Lazarian 1998) which emit however more in the millimeter (mm) range (Bot et al. 2010).

A step forward has been the possibility to carry out spatially resolved analysis of the dust SED with a combination of *Spitzer* and *Herschel* data, which allow to investigate variations of the dust properties at small scales. The Magellanic Clouds and M33 are excellent targets to perform such studies. In the Large Magellanic Cloud (LMC) Galliano et al. (2011) found evidence for a submm excess in the low surface brightness areas by fitting the dust SED locally with a detailed dust model. Gordon et al. (2014) were able to fit the SEDs of the LMC and the Small Magellanic Cloud (SMC) using a MBB with a broken power-law for β . For M33 Tabatabaei et al. (2014) carried out a MBB fit of the local SED and found a trend of decreasing temperature T and decreasing β with radius (this trend is the opposite of what would be expected from the β - T degeneracy). They concluded that a change in the dust properties is the most likely reason for this trend. Other studies have tried to look for variations in the dust properties in further objects. Galametz et al. (2014) investigated the 870 μ m emission of a sample of 11 nearby galaxies and found evidence for a submm excess in 4 of them. For three of these objects the excess was in the outskirts of the galaxy. Hermelo et al. (2013) decomposed the observed emission of the dwarf, low metallicity galaxy NGC 4214 into its SF and diffuse components. They modeled these components separately using radiation transfer models and found indications of submm excess in the diffuse component of NGC 4214.

This paper is part of a series of studies that use radiation transfer models to fit the SED of a sample of dwarf starburst and late-type spiral disk galaxies. Here we apply the same methodology as in Hermelo et al. (2013) to the local-group galaxy M33. The proximity of M33 (0.840 Mpc, Freedman et al. 1991), its moderate inclination angle (57°, Deul & van der Hulst 1987) and the wide data set available, make this galaxy an excellent target to study separately the SEDs of the SF and the diffuse component with accuracy. Recent results of the open time key

program HerM33es (Kramer et al. 2010) have shown that the *Herschel* observations of M33 can not be well reproduced assuming standard dust properties (i.e. MBB model with $\beta=2$). Instead, these authors had to adopt a MBB model with $\beta=1.5$ to obtain a good fit. The value of $\beta=1.5$ is extensible to the *Planck* data (see Appendix A for details) and suggests that the dust properties or conditions might be special in M33.

The aim of the present paper is to investigate if it is possible to reproduce the SED of M33 with standard dust grain properties but using more sophisticated models based on radiation transfer calculations and a realistic geometry, or if the anomalies found by Kramer et al. (2010) persist. The paper is organized as follows. In Sect. 2 we present the data set used, from UV to radio. Sect. 3 is devoted to explain the photometry measurements and the method we have used to separate the emission coming from the SF regions and the ISM in the galaxy. In Sect. 4 we explain briefly the models applied to fit the SED of the two components and how we determined their input parameters. The results of the modeling are presented in Sect. 5. In Sect. 6 we discuss the results and in Sect. 7 we summarize the main conclusions of this paper.

2. Data

A wide range of data from recent scientific missions are available for M33 in archives. In this section we describe the data used in our study, which are summarized in Tab. 1.

2.1. GALEX

To investigate the continuum UV emission associated with the young stellar population of M33, we use the data from the *Galaxy Evolution Explorer* (GALEX, Martin et al. 2005) distributed by Gil de Paz et al. (2007). The GALEX far-UV (FUV ~ 154 nm) and near-UV (NUV ~ 232 nm) observations and the data reduction can be found in Thilker et al. (2005). The angular resolution for the GALEX FUV and NUV maps is 4''2 and 5''3, respectively. Following Morrissey et al. (2007), we conservatively adopted a calibration error of 10%.

2.2. Sloan

We used data from the Sloan Digital Sky Survey (SDSS, York et al. 2000) to measure the stellar emission in the u -band and to calculate the b -band stellar disk scale-length of M33. Due to the small FoV of the SDSS images, we needed to reconstruct a mosaic to cover the whole extension of M33 in these bands. For this purpose, we used the software Montage¹. Montage is a toolkit for creating mosaics from individual Flexible Image Transport System (FITS) images. We made use of the data from the seventh data release (DR7, Abazajian et al. 2009). These images have a spatial coverage of 13'51 \times 9'83, an exposure time of 53.9 s, and the angular resolution is $\sim 1''.4$ (median value measured in the *Sloan r*-band). The SDSS DR7 pipeline does not apply any sky subtraction to the raw data. Considering that most of the frames used to reconstruct the mosaics are fully covered by light coming from M33, the usage of the DR7 data allows us to avoid possible artifacts coming from an inaccurate sky subtraction. Following Padmanabhan et al. (2008) we adopted 1% of calibration error for the *Sloan g*-band and 2% for the *Sloan u*-band.

¹ <http://montage.ipac.caltech.edu>

Telescope	Instrument or filter	λ_0 μm	ν_0 GHz	FWHM	Δ_{CAL} %	Band name	References
<i>GALEX</i>	FUV	0.154	1 946 704	4''2	10	<i>GALEX</i> FUV	Thilker et al. (2005)
	NUV	0.232	1 292 209	5''3	10	<i>GALEX</i> NUV	Thilker et al. (2005)
<i>Sloan</i>	<i>u</i>	0.355	844 486	1''4	2	<i>Sloan u</i> -band	This paper.
	<i>g</i>	0.469	639 216	1''4	1	<i>Sloan g</i> -band	This paper.
<i>KPNO</i>	H α	0.657	456 305	6''6	15	H α	Greenawalt (1998)
<i>Spitzer</i>	IRAC	3.55	84 449	2''5	2	IRAC 3.6 μm	Verley et al. (2007)
	IRAC	4.49	66 769	2''9	2	IRAC 4.5 μm	Verley et al. (2007)
	MIPS	23.7	12 650	6''3	4	MIPS 24 μm	This paper.
<i>Herschel</i>	PACS	70.0	4 283	5''6	10	PACS 70 μm	Boquien et al. (2015)
	PACS	100	2 998	9''8	10	PACS 100 μm	Boquien et al. (2011)
	PACS	160	1 874	13''6	20	PACS 160 μm	Boquien et al. (2011)
	SPIRE	250	1 199	18''1	5	SPIRE 250 μm	Xilouris et al. (2012)
	SPIRE	363	826	24''9	5	SPIRE 350 μm	Xilouris et al. (2012)
	SPIRE	517	580	36''4	5	SPIRE 500 μm	Xilouris et al. (2012)
<i>APEX</i>	LABOCA	870	345	19''2	10	LABOCA 870 μm	Albrecht et al. (in prep.)
<i>Planck</i>	HFI	350	857	4'63	10	PLANCK 350 μm	This paper.
	HFI	550	545	4'84	10	PLANCK 550 μm	This paper.
	HFI	850	353	4'86	3	PLANCK 850 μm	This paper.
	HFI	1 380	217	5'01	3	PLANCK 1.4 mm	This paper.
	HFI	2 096	143	7'27	3	PLANCK 2.1 mm	This paper.
	HFI	3 000	100	9'66	3	PLANCK 3.0 mm	This paper.
	LFI	10 000	30	32'3	3	PLANCK 10 mm	This paper.
<i>Effelsberg</i>	S 36 mm	35 903	8.35	1'39	*	S 36 mm	Tabatabaei et al. (2007b)

Table 1: Summary of the observations used in this study. *Only the total error is reported in Tabatabaei et al. (2007b).

2.3. H α

To trace the ionized gas, we use the narrow band H α image of M33 obtained with the Kitt Peak National Observatory (KPNO) by Greenawalt (1998). The reduction process, using standard IRAF² procedures to subtract the continuum emission, is described in detail in Hoopes & Walterbos (2000). The total field of view (FoV) of the image is $1.75 \times 1.75 \text{ deg}^2$ (2048×2048 pixels with a pixel scale of $2''.03$) with a $6''.6$ resolution. We consider typical uncertainties to be better than 15% for the H α photometric measurements (Verley et al. 2010b).

2.4. Spitzer

Data of M33 was obtained with the *Spitzer* (Werner et al. 2004) Infrared Array Camera (IRAC, Fazio et al. 2004) and the Multiband Imaging Photometer (MIPS, Rieke et al. 2004). We use IRAC 3.6 μm and 4.5 μm data to study the radiation field as-

sociated with the old stellar population of M33 and MIPS 24 μm to study the dust emission. The MIPS 70 μm and MIPS 160 μm data were not used in this work since better quality data from PACS are available at the same wavelengths. The emission from polycyclic aromatic hydrocarbons (PAHs), traced by the IRAC 5.8 μm and 8.0 μm bands, is out of the scope of the present work.

IRAC 3.6 μm and 4.5 μm data are described in Verley et al. (2007, 2009, 2010a). The MIPS 24 μm data have been processed using the version 18.5 of the MOPEX software (MOsaicker and Point source EXtractor, Makovoz & Marleau 2005) to combine the 16 AORs (Astronomical Observation Request) available in the data archive. The spatial resolution is $2''.5$, $2''.9$, and $6''.3$ for the IRAC 3.6 μm , IRAC 4.5 μm , and MIPS 24 μm bands, respectively. We adopted calibration errors of 2% and for the IRAC bands (Reach et al. 2005) and 4% for MIPS 24 μm (Engelbracht et al. 2007).

2.5. Herschel

As part of the HerM33es key program (Kramer et al. 2010), the M33 galaxy was mapped by *Herschel* with the Photodetector

² IRAF is distributed by the National Optical Astronomy Observatories, which are operated by the Association of Universities for Research in Astronomy, Inc., under cooperative agreement with the National Science Foundation.

Array Camera and Spectrometer (PACS, Poglitsch et al. 2010) and the Spectral and Photometric Imaging Receiver (SPIRE, Griffin et al. 2010). PACS 100 μm and 160 μm and SPIRE 250 μm , 350 μm , and 500 μm observations were done in parallel mode in two orthogonal directions on January 7th, 2010, covering a region of about 1.36 square degrees. The PACS 70 μm image was obtained as a follow-up open time cycle 2 programme, on 25 June 2012 in 2 orthogonal directions and 5 repetitions to achieve better sensitivity (Boquien et al. 2015). The PACS reduction has been performed using the map-making software Scanamorphos (Roussel 2013) as described in Boquien et al. (2011). The SPIRE reduction has been done using the *Herschel* Data Processing System (HIPE, Ott 2010, 2011) and the maps were created using a "naive" mapping projection (Verley et al. 2010b; Boquien et al. 2010; Xilouris et al. 2012). The angular resolution of the *Herschel* data range from 5''.6 at 70 μm to 36''.4 for the 500 μm band. The absolute photometric uncertainty is 10% for the PACS 70 μm and 100 μm bands and 20% for the PACS 160 μm band (Poglitsch et al. 2010), while we adopted 5% as the calibration uncertainty for the three SPIRE bands (Bendo et al. 2013).

2.6. LABOCA

Observations of M33 were carried out at the Atacama Pathfinder Experiment (APEX, Güsten et al. 2006) using the Large Bolometer Camera (LABOCA, Siringo et al. 2009) between 2010 and 2012 (Albrecht et al., in prep.). A filter set coupled to the atmospheric window provides a bandwidth of $\sim 150 \mu\text{m}$ ($\sim 60 \text{ GHz}$) around the central frequency of 870 μm (345 GHz). From observations of Uranus an almost circular beam size of $19''.2 \pm 0''.7$ was determined (Siringo et al. 2009). LABOCA mapping was performed in on-the-fly mode parallel and orthogonal to the major axis of M33. Flux calibration was achieved through observations of planets as well as a set of secondary calibrators and was found to be accurate within 10% (Siringo et al. 2009). To enable the usage of the LABOCA data in multi-wavelength studies the flux calibration methods for LABOCA and SPIRE were compared to ensure a correct cross-calibration. On average 2% lower flux densities from the LABOCA calibration compared to the SPIRE method were found.

The LABOCA data were reduced using the BoA³ software package. The applied skynoise suppression can not distinguish between correlated atmospheric noise and astronomical emission that is uniformly extended over areas equal to or larger than the area covered by the groups of bolometer channels (defined by having the same amplifier box or same wiring) that are used to derive the median noise. This typically filters out uniform emission on scales larger than about 2'.5 (for details see Schuller et al. 2009). To minimize the effect an iterative approach by subsequently improving a model of the flux distribution was applied. Nevertheless, given the large apparent size of M33, the resulting LABOCA map does not recover the entire contribution from the extended emission, as it is confirmed by comparing with the corresponding PLANCK 850 μm map (see Fig. 1).

2.7. Planck

We used *Planck* data from the 2013 distribution of released products (Planck Collaboration et al. 2014a) based on the data acquired during the *Planck* "nominal" operations period, i.e., be-

tween 12 August 2009 and 27 November 2010. Data can be accessed via the *Planck* Legacy Archive⁴.

In the case of the Low Frequency Instrument (LFI) 10 mm (30 GHz) band, we used the flux computed in the *Planck* Catalog of Compact Sources (Planck Collaboration et al. 2014c). For the other *Planck* bands, i.e., the High Frequency Instrument (HFI) 350 μm (857 GHz), 550 μm (545 GHz), 850 μm (353 GHz), 1.4 mm (217 GHz), 2.1 mm (143 GHz), and 3.0 mm (100 GHz) bands and the LFI 4.3 mm (70 GHz) and 6.8 mm (44 GHz) bands, we extracted the fluxes from the *Planck all-sky* maps. These maps consist of 2048 HEALPix full-sky maps (Górski et al. 2005) corresponding to a pixel size of 2'.64 with an angular resolution that ranges from 4'.63 at 350 μm to 32'.3 at 10 mm (Ade et al. 2014). To generate a Gnomonic projection of the HEALPix data centered on M33 we made use of the IDL facility Gnomview⁵. The cosmic microwave background (CMB) was subtracted from all the bands (see Appendix B for details). The contribution from other components (e.g., cirrus, cosmic infrared background) to the background was subtracted as the median value in a 5' width annulus enclosing M33. The resulting maps are shown in Fig. 1. M33 was not detected in the 4.3 mm and 6.8 mm channels. We adopted $\pm 10\%$ of calibration uncertainty for the 350 μm and 550 μm bands and $\pm 3\%$ for all the other wavelengths (Ade et al. 2014).

2.8. Effelsberg

Tabatabaei et al. (2007a) studied the emission at 3.6 cm (8.35 GHz) of M33. Here we used their results to constrain the thermal radio emission of the SF regions as well as to decontaminate our measurements from synchrotron emission (see Sect. 3.3 for details).

They found a total flux of $761 \pm 63 \text{ mJy}$ for the inner 7.5 kpc and a thermal fraction of $51.4 \pm 4.2\%$ at this wavelength. This fraction was obtained from the extinction corrected H α map of the galaxy, which was derived using a map of optical depth at 160 μm and an extinction law for a standard dust model for the diffuse emission. The authors also derived the thermal fraction using the classical method and assuming a constant non-thermal spectral index for the whole galaxy of $\alpha_n = 1.0 \pm 0.1$. With this method they obtained a thermal fraction of $63.2 \pm 5.3\%$.

As a compromise between the two values of the thermal fraction derived by Tabatabaei et al. (2007a), we adopted the mean value as the best estimate and we allowed it to fluctuate between the lowest and the highest possible values. We therefore estimated that $57.3 \pm 11.2\%$ ($436 \pm 49 \text{ mJy}$) of the total flux at 8.35 GHz corresponds to thermal radio emission.

3. Photometry

Prior to performing the photometry, we first homogenized all the images to the same data unit in order to measure all fluxes in Jy/pixel (with a pixel size of 14''). Bright foreground stars were removed from the UV and optical data. We then convolved all the data to the resolution of SPIRE 500 μm using the set of kernels provided by Aniano et al. (2011)⁶, with the only exception of *Planck* data, which have a coarser resolution than the SPIRE 500 μm image, and therefore, they were only used to obtain the total photometry of M33. Using the IRAF task

⁴ http://www.sciops.esa.int/index.php?project=planck&page=Planck_Legacy_Archive

⁵ <http://healpix.jpl.nasa.gov/html/idlnode21.htm>

⁶ <http://www.astro.princeton.edu/ganiano/Kernels.html>

³ <http://www.astro.uni-bonn.de/boawiki/Boa>

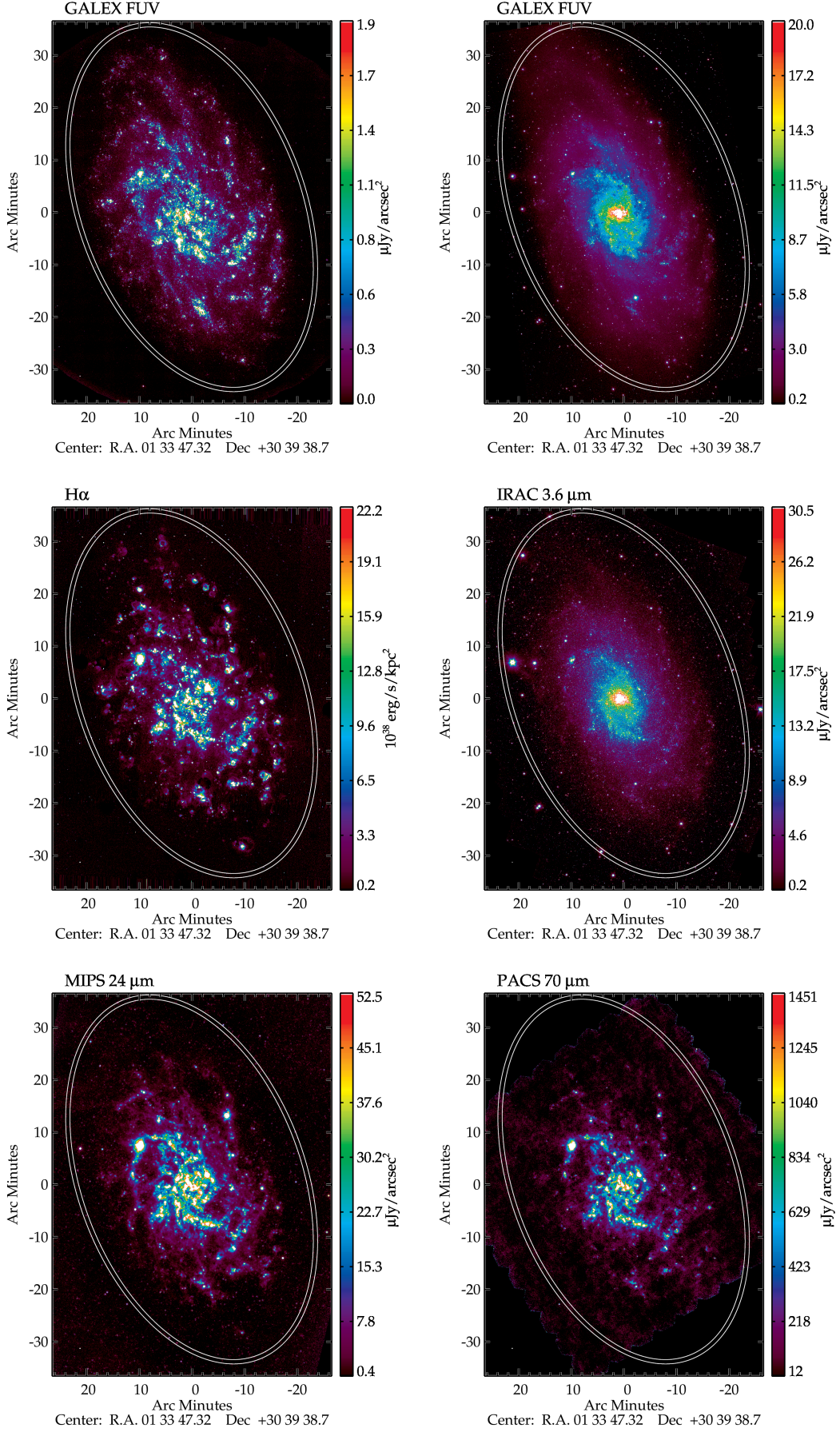


Fig. 1: Data of M33 at their original resolution. Units have been homogenized to facilitate the comparison between the different bands. At the distance of M33, $1''$ subtends ~ 4 pc. The white annulus, used to subtract the local background, has been included for reference. The white circle at the left bottom (too tiny to be visible for bands with $\lambda \lesssim 350 \mu\text{m}$) corresponds to the beam size.

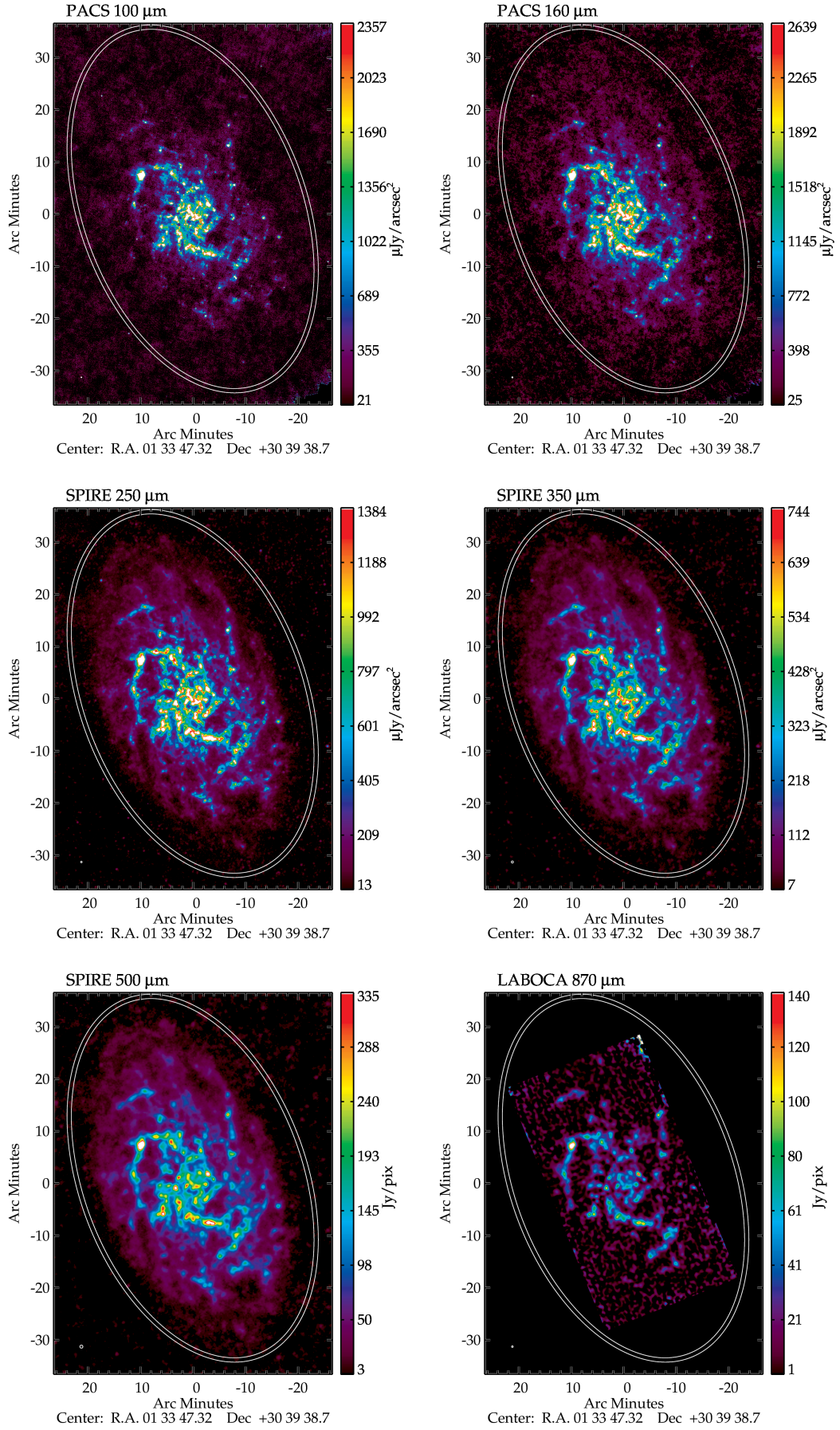


Fig. 1: Continued.

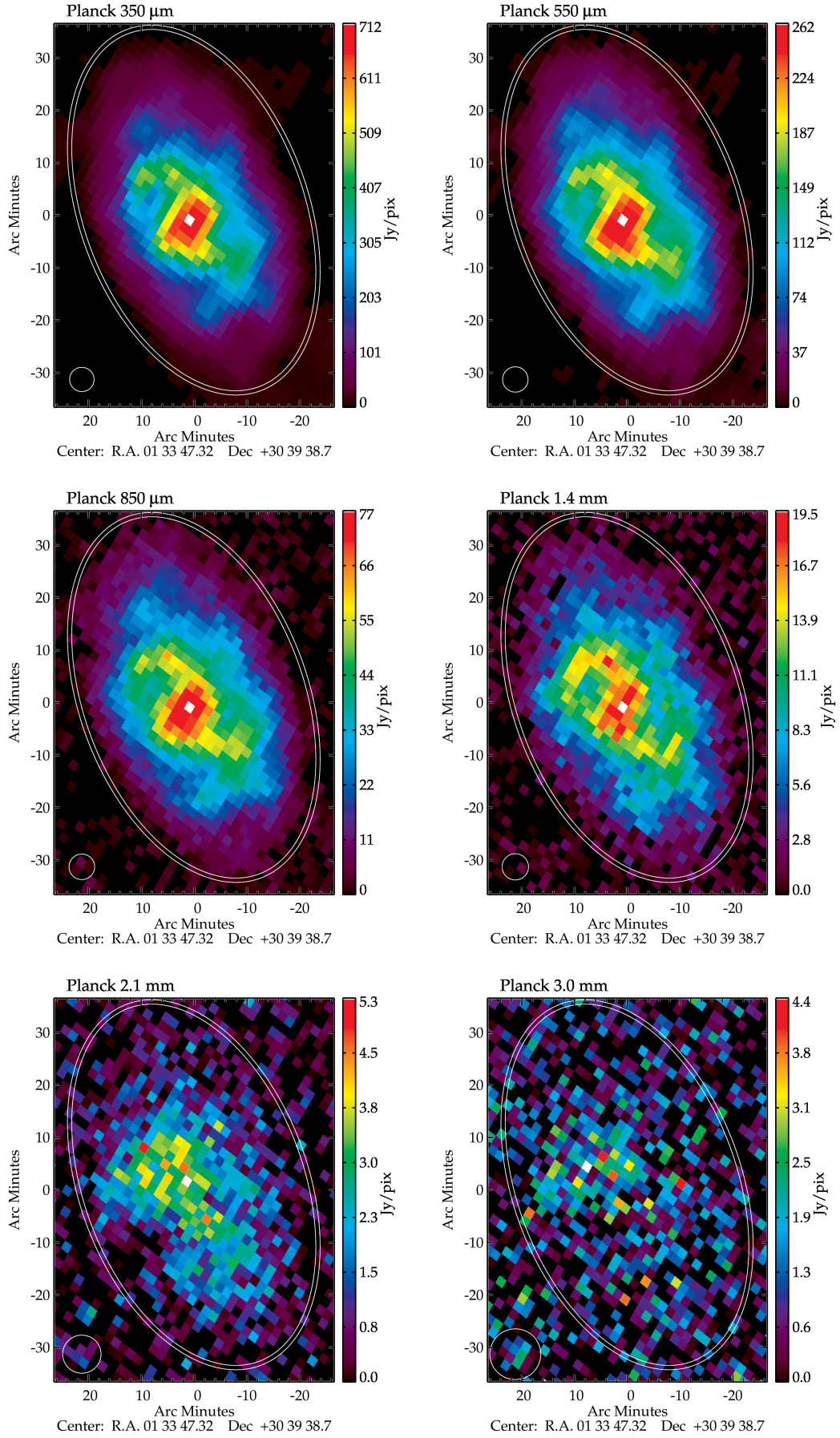


Fig. 1: Continued.

wregister, we then regridded all the images to the pixel size of the SPIRE 500 μm map. Color corrections were applied to all the MIR/FIR/submm/mm fluxes (see Appendix A for details). In this section we describe how we separated the different components, how we corrected our measurements from undesired contributions (e.g., CO line emission), and how the errors were handled.

3.1. Component separation

In order to decompose M33 into its SF and diffuse components, we used the software SExtractor (Bertin & Arnouts 1996). SExtractor explores a given image for knots of emission by searching groups of connected pixels that exceed some threshold above the background in the surroundings of the region.

We run SExtractor on the $H\alpha$ image in order to separate the SF from the diffuse component. As the diffuse emission reaches a higher level in the inner part than in the outskirts of the galaxy, the threshold should be relative and vary to reflect these local variations. The size of the background mesh should be large enough to avoid a strong contamination from the SF but small enough to reproduce the local scale variations of the diffuse emission. We find that a mesh size of 12 pixels (with a pixel size of 14'' this corresponds to 680 pc) yields an adequate separation between the detected SF objects and background map accounting for the diffuse emission. In practice, the decomposition between the SF and diffuse components can be summarized in two main steps. Firstly, the diffuse emission map is computed by estimating the background (using a clipping to reject the bright SF regions) in each cell of a grid that covers the whole image. Secondly, SF regions are detected above a local threshold equal to 40 times the background noise map obtained in the previous step. The result of this separation method is shown in Fig. 2.

We tested different local thresholds between 5 and 100 times the background noise. We found that for values below 20 the SF regions detected are significantly contaminated by diffuse emission. On the other hand, values above 60 produces the rejection of many of the fainter SF regions. A good compromise that leads to an optimal separation of the two components was found for a threshold of 40. We adopted this intermediate value and we discuss in Appendix C the impact of our choice.

To replicate the same separation in the other bands, we first derive a map of the diffuse emission in the same way as done for the $H\alpha$ map. We then obtain the difference between each original image and its diffuse emission map to remove the background/foreground diffuse emission from the whole map. Subsequently, we create a mask mirroring the detected SF objects in the $H\alpha$ image and applied it to the full set of multiwavelength images to extract the exact same SF regions in all the bands, without being contaminated by the diffuse emission. We used the $H\alpha$ image to create the mask because this is the band that best represents the wavelength-dependent morphology of the SF regions. Finally, for each band, the diffuse emission map is obtained by subtracting the SF region map to the original map.

Once the SF and diffuse component are separated for each band we determined the flux densities by integrating over the corresponding maps (see Tab. 2). We used an aperture for the entire galaxy defined by a radius of 35' (8.5 kpc) and an inclination of 57° (see Fig. 1). This aperture is slightly larger than the one used by Kramer et al. (2010) in order to enclose the whole emission of the Planck bands, which have a much poorer resolution than the data used by these authors.

In those cases where the angular resolution did not allow to extract the emission from the SF regions (i.e., Planck data),

the diffuse emission was estimated by subtracting the flux of the SF component predicted by the model of Groves et al. (2008) from the total flux of M33. Even though our estimates of the diffuse emission are well constrained by this method in most wavelengths, the lack of data points constraining the SED of the SF component between LABOCA 870 μm and the free-free emission at 3.6 cm from Tabatabaei et al. (2007a) introduces some uncertainties. As a cautionary measure, we do not include the indirect data points in the fitting procedure.

3.2. CO contamination

The emission from the CO rotational transitions CO(1 \rightarrow 0) at 2.6 mm (115 GHz), CO(2 \rightarrow 1) at 1.3 mm (230 GHz), and CO(3 \rightarrow 2) at 870 μm (345 GHz), fall into the bandpasses of the Planck 3.0 mm, 1.4 mm, and 850 μm filters, respectively (Planck Collaboration et al. 2014b). In addition, the LABOCA 870 μm filter is also affected by the CO(3 \rightarrow 2) line.

In order to correct the measured continuum fluxes for the contribution of these major gas cooling lines, we made use of CO(2 \rightarrow 1) observations (Druard et al. 2014) obtained with the Heterodyne Receiver Array (HERA, Schuster et al. 2004) mounted on the IRAM 30 m telescope on Pico Veleta (Spain).

Druard et al. (2014) mapped the inner ~ 7 kpc of M33 with an angular resolution of 12''. These authors reported a total CO(2 \rightarrow 1) luminosity of $2.8 \times 10^7 \text{ K km s}^{-1} \text{ pc}^2$, which corresponds to a flux of $6.5 \times 10^4 \text{ Jy km s}^{-1}$. For the PLANCK 1.4 mm filter, which has a width of 64.5 GHz ($87\,433 \text{ km s}^{-1}$) and a transmission close to 100% at the frequency of the CO(2 \rightarrow 1) line (see Fig. 1 in Planck Collaboration et al. 2014b), we measured a flux density of 17.4 Jy. Using these values we estimate that 4.3% of the flux density of M33 measured with this filter comes from CO(2 \rightarrow 1) line emission.

The CO(1 \rightarrow 0) line emission was also observed with the IRAM 30 m telescope in a radial cut along the major axis of M33 (Braine et al. 2010). Comparing these data with their map, Druard et al. (2014) found a constant ratio $I_{\text{CO}(1\rightarrow 0)}/I_{\text{CO}(2\rightarrow 1)}$ of 1.25 in the overlapping area. Assuming that this ratio can be extrapolated to the whole disk of M33, we can estimate the flux of CO(1 \rightarrow 0) as:

$$S_{\text{CO}(1\rightarrow 0)} = 1.25 \times \left(\frac{115}{230}\right)^2 S_{\text{CO}(2\rightarrow 1)} = 2.0 \times 10^4 \text{ Jy km s}^{-1}. \quad (2)$$

We measured a flux density of 1.56 Jy with the PLANCK 3.0 mm filter, which has a width of 32.9 GHz ($97\,762 \text{ km s}^{-1}$) and a transmission of about 60% at the frequency of the line. Therefore, we estimate that the CO(1 \rightarrow 0) emission is responsible for 7.9% of the flux measured with the PLANCK 3.0 mm band.

Finally, the contamination due to the emission from the CO(3 \rightarrow 2) line was estimated assuming a ratio $I_{\text{CO}(3\rightarrow 2)}/I_{\text{CO}(2\rightarrow 1)} \sim 1$, i.e.:

$$S_{\text{CO}(3\rightarrow 2)} \sim \left(\frac{345}{230}\right)^2 S_{\text{CO}(2\rightarrow 1)} = 14.6 \times 10^4 \text{ Jy km s}^{-1}. \quad (3)$$

With the PLANCK 850 μm filter we measured a flux density of 74.3 Jy. Using a width of 101.4 GHz ($85\,032 \text{ km s}^{-1}$) and a transmission $\sim 100\%$, we found that the contribution from the CO(3 \rightarrow 2) line to the PLANCK 850 μm is $\sim 2.3\%$. In the case of the LABOCA 870 μm filter, we measured a flux density of 37.1 Jy. For a width of 59.8 GHz ($52\,026 \text{ km s}^{-1}$) and a transmission $\sim 100\%$, we found that the contribution from the CO(3 \rightarrow 2) line to this filter is ($\sim 7.6\%$).

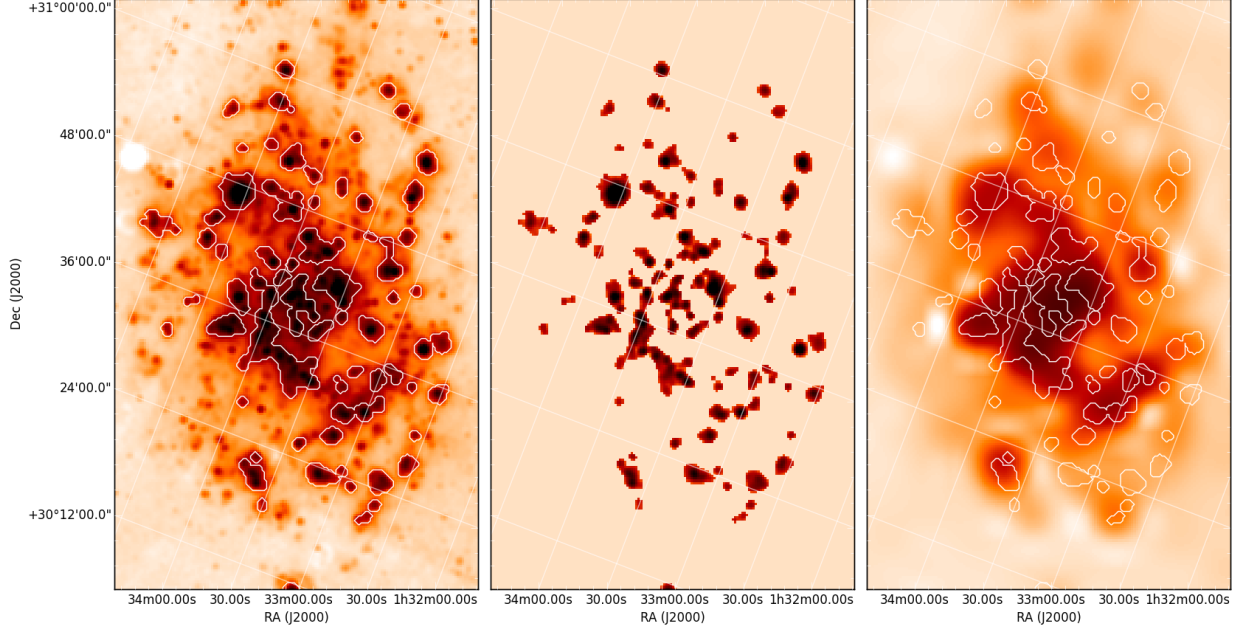


Fig. 2: Example of the component separation method for the case of the $H\alpha$ emission. The left panel is the original $H\alpha$ image smoothed to the resolution of the SPIRE $500\mu\text{m}$ band, the central panel shows the SF regions detected by **SExtractor** using a threshold of 40, and the right panel corresponds to the diffuse emission. The white contours are included to facilitate the comparison between panels and they correspond to the boundaries of the SF regions. The emission from the SF component represents 41.7% of the total $H\alpha$ emission.

3.3. Synchrotron emission

Unlike the free-free emission coming from the $H\text{II}$ regions, the modeling applied in this work does not take into account the contribution of the synchrotron emission. For this reason, the fluxes measured with *Planck* need to be decontaminated from this component. Following the analysis of Tabatabaei et al. (2007a) we extrapolated the synchrotron emission from 3.6 cm to the *Planck* filters assuming a non-thermal spectral index of 0.72 (see Sect. 2.8). We found non-thermal contributions of 30% and 5% respectively for the *PLANCK* 10 mm and 3.0 mm bands, while for the other bands this contribution was found to be negligible.

3.4. Error of flux measurements

In our error analysis we took two types of error into account: i) calibration, Δ_{cal} , using the values presented in Tab. 1, and ii) measurement error due to background fluctuations, Δ_{back} .

The error due to the background fluctuations was calculated by assuming that each pixel within the aperture has an error given by the standard deviation of the background noise, σ_{back} . In addition, we have to take the error of the background into account which was subtracted within an aperture of N_{apert} pixels. This error is $\sigma_{\text{back}}N_{\text{apert}}/\sqrt{N_{\text{back}}}$, where N_{back} is the number of pixels used to compute the level of background. This gives (see also Dale et al. 2012) a total error for the background subtracted flux of

$$\Delta_{\text{back}} = \sigma_{\text{back}} \sqrt{N_{\text{apert}} + \frac{N_{\text{apert}}^2}{N_{\text{back}}}}. \quad (4)$$

The final error for the flux is the quadratic sum of Δ_{cal} and Δ_{back} . In the case of the *Planck* data, Δ_{back} also includes the error due to the CMB subtraction.

4. Models for the dust emission

We analyzed the full UV to radio SED of the different emission components of the galaxy using the radiation transfer model of Popescu et al. (2011), which self-consistently treats the dust emission from the SF and the diffuse components, considering the illumination of the diffuse dust both by the distributed stellar populations and by the escaping light from the $H\text{II}$ regions. While maintaining consistency within the framework of the Popescu et al. (2011) model, we used the model of Groves et al. (2008) to provide a detailed description of the dust emission from the SF component. The methodology used in this work is similar to the one applied to the low-metallicity, dwarf galaxy NGC 4214 in Hermelo et al. (2013). For a detailed description of the models we refer the reader to Groves et al. (2008) and Popescu et al. (2011). To make this paper self-contained, in the following sections we present a brief description of the physics and parameters of the models.

4.1. The model of Popescu et al. (2011)

Popescu et al. (2011) present a self-consistent model based on full radiative transfer calculations of the propagation of starlight in disk galaxies. These authors adopted the dust properties from Weingartner & Draine (2001) and Draine & Li (2007), incorporating a mixture of graphite, silicate, and PAH molecules. To

BAND	$S_{\text{TOT}}^{\text{obs}}$ (Jy)	$S_{\text{SF}}^{\text{obs}}$ (Jy)	$S_{\text{DIFF}}^{\text{obs}}$ (Jy)	$S_{\text{SF}}^{\text{obs}}/S_{\text{TOT}}^{\text{obs}}$ (%)
<i>GALEX</i> FUV	2.40 \pm 0.27	-	-	-
<i>GALEX</i> NUV	3.52 \pm 0.39	-	-	-
<i>Sloan</i> <i>u</i> -band	5.93 \pm 0.32	-	-	-
H α	0.09 \pm 0.02	0.04 \pm 0.007	-	41.7
IRAC 3.6 μm	23.7 \pm 1.26	-	-	-
IRAC 4.5 μm	15.3 \pm 0.82	-	-	-
MIPS 24 μm	47.6 \pm 3.05	19.6 \pm 1.25	29.2 \pm 2.37	41.2
PACS 70 μm	578 \pm 64.7	223 \pm 25.0	349 \pm 42.8	38.7
PACS 100 μm	1387 \pm 155	360 \pm 40.3	1026 \pm 125	26.0
PACS 160 μm	2162 \pm 445	381 \pm 78.6	1773 \pm 376	17.6
SPIRE 250 μm	1316 \pm 86.8	197 \pm 13.1	1111 \pm 92.0	15.0
PLANCK 350 μm	777 \pm 89.5	-	684 \pm 78.8	12.0
SPIRE 350 μm	718 \pm 47.4	90.5 \pm 5.97	632 \pm 52.3	12.6
SPIRE 500 μm	319 \pm 21.0	37.5 \pm 2.47	279 \pm 23.1	11.7
PLANCK 550 μm	305 \pm 35.1	-	279 \pm 32.2	8.3
PLANCK 850 μm	91.9 \pm 6.91	-	85.7 \pm 6.45	6.8
LABOCA 870 μm	-	10.0 \pm 1.12	-	-
PLANCK 1.4 mm	21.7 \pm 1.95	-	20.3 \pm 1.83	6.5
PLANCK 2.1 mm	4.27 \pm 0.57	-	3.66 \pm 0.49	14.2
PLANCK 3.0 mm	1.86 \pm 0.19	-	1.41 \pm 0.14	24.2
PLANCK 10 mm	0.40 \pm 0.09	-	-	-
S 36 mm	0.44 \pm 0.05	0.44 \pm 0.05	-	100.0

Table 2: Flux densities of M33 measured for the different bands. The total emission ($S_{\text{TOT}}^{\text{obs}}$) is shown in column 2. Columns 3 and 4 correspond to the emission from the SF ($S_{\text{SF}}^{\text{obs}}$) and the diffuse ($S_{\text{TOT}}^{\text{obs}}$) component. Column 5 indicates the percentage of the total flux emitted by the SF component.

approximate the large-scale geometry of the galaxy (see Fig. 1 in Popescu et al. 2011), they use two separate components:

- An old component consisting of an old stellar disk, an old stellar bulge, and a thick disk of dust.
- A young component consisting of a young stellar disk and a thin disk of dust.

The spectral energy distribution of both old and young stellar components are shown in Tab. E.2 and in Fig. 8 of Popescu et al. (2011). These authors only considered the optical-IR radiation for the old stellar population, and neglected any contribution in the UV. The spectral distribution covers the wavelengths from 4 430 Å to 50 000 Å. The young stellar population is defined as an exponentially declining *SFR* with a time constant of 5 Gyr, solar metallicity and Salpeter IMF with an upper mas cut-off of 100 M_{\odot} . The spectral distribution covers from 912 Å to 50 000 Å.

Apart from the diffuse component, the model includes a clumpy component, consisting of the parent molecular clouds of young (≤ 10 Myr) and massive stars. This component will be modeled here in a different way than Popescu et al. (2011) have done (see Sect. 4.2), as for M33 it is possible to separate the emission from the SF regions and the diffuse dust.

The input parameters of the Popescu et al. (2011) model are:

- The total central face-on B-band opacity, $\tau_{\text{B}}^{\text{f}}$.
- The star formation rate, *SFR*.
- The clumpiness factor *F*, which is linked to the fraction of photons that escape (f_{esc}) from the SF regions into the diffuse medium ($F=1-f_{\text{esc}}$).
- The normalized luminosity of the old stellar disk, *old*.
- The bulge-to-disk ratio, *B/D*.
- The radial scale length of the old stellar disk, h_{s} . All other spatial scales in the galaxy related to the different component in the model have a constant ratio with h_{s} (see Tab. E.1 in Popescu et al. 2011).
- The inclination angle of the galaxy, *i*.

From the primary parameters *SFR* and *F*, Popescu et al. (2011) define the SFR powering the diffuse emission, *SFR'*, as follows (Eq. 45 in Popescu et al. 2011):

$$SFR' = SFR \times (1 - F). \quad (5)$$

The library of diffuse SEDs of Popescu et al. (2011) contains results for a four-dimensional parameter space spanned by $\tau_{\text{B}}^{\text{f}}$, *SFR'*, *old*, and *B/D*.

The diffuse component is calculated as an extrinsic quantity corresponding to a reference size (corresponding to a reference

scalelength). To scale the intensity of the radiation field heating the diffuse dust, the parameters SFR' and old must be scaled to the reference size by comparing the scalelengths (Eq. D.3 in Popescu et al. 2011):

$$SFR^{\text{mod}} = SFR' \times \left(\frac{h_{\text{ref}}}{h_s} \right)^2, \quad (6)$$

$$old^{\text{mod}} = old \times \left(\frac{h_{\text{ref}}}{h_s} \right)^2, \quad (7)$$

where $h_{\text{ref}}=5670$ pc is the reference B-band scalelength, h_s is the B-band scalelength of the galaxy under study, and SFR^{mod} and old^{mod} are internal parameters that allow us to interface with the library of models. An additional scaling is required to set the flux levels of the SEDs from the library, $S_v^{\text{d,mod}}$, to the SED that represents our galaxy, S_v^{d} :

$$S_v^{\text{d}} = \left(\frac{h_s}{h_{\text{ref}}} \right)^2 \times S_v^{\text{d,mod}}, \quad (8)$$

where $S_v^{\text{d,mod}}$ is determined by the parameters τ_B^f , SFR^{mod} , old^{mod} , and B/D (Popescu et al. 2011, Eq. D.2). We would like to stress that in these models the absolute flux level of the predicted dust SED is fixed by the input parameters.

In the model of Popescu et al. (2011), the stellar radiation field leaving the galaxy, S_v^s , can be calculated as:

$$S_v^s = S_v^{\text{s,int}} 10^{-\Delta m_\lambda/2.5}, \quad (9)$$

where $S_v^{\text{s,int}}$ is the intrinsic stellar radiation field, and Δm_λ is the composite attenuation. In the case of the UV and optical emission coming from the young stellar population, Δm_λ can be written as:

$$\Delta m_\lambda \simeq -2.5 \log(1 - F f_\lambda) + \Delta m_\lambda^{\text{disk}}. \quad (10)$$

The first part of Eq. 10 takes into account the attenuation in the SF component, while $\Delta m_\lambda^{\text{disk}}$ is responsible for the attenuation in the diffuse component. The wavelength dependence of the escape fraction, f_λ , is tabulated in Tuffs et al. (2004, Tab. A.1). Therefore, by combining Eq. 9 and Eq. 10, it is possible to calculate the radiation field associated with the young stellar population that escapes the galaxy ($S_v^{\text{s,young}}$). The emission of the old stars that leaves the galaxy ($S_v^{\text{s,old}}$) is calculated in a similar way, but in this case the composite attenuation is $\Delta m_\lambda = \Delta m_\lambda^{\text{disk}}$, since this radiation field is only attenuated by the diffuse ISM.

It is noteworthy that in the Popescu et al. (2011) model the old stellar population emits exclusively in the optical-IR wavelength range (see their Tab. E.2), i.e., the emission corresponds to the radiation field emitted by a remarkably old stellar population. Thus, what Popescu et al. (2011) calls 'old' stellar population does not correspond to the definition of 'old' stellar population usually found in the literature (see the Fig. 1 panel Scd of Rowan-Robinson et al. 2008 for an example of a moderate old stellar population with a SED extending into the optical-UV range). As a consequence, in the Popescu et al. (2011) model the old stellar population has little relevance for the dust heating.

4.2. The model of Groves et al. (2008)

In Popescu et al. (2011) the clumpy component corresponding to the SF regions is modeled with an average template representing the emission of all SF regions. Although this is a good approach

for unresolved galaxies, the high spatial resolution of our data allowed us to apply a detailed modeling of the SF component.

The Groves et al. (2008) model describes the luminosity evolution of a star cluster of mass M_{cl} , and incorporates the expansion of the H II region and PDR due to the mechanical energy input of stars and supernovae. The dust emission from the H II region and the surrounding PDR is calculated from radiation transfer calculations. The hydrogen column density of the PDR is fixed to the value $N_{\text{HI}}^{\text{PDR}}=10^{22} \text{ cm}^{-2}$. The Groves et al. (2008) model assumes a standard mixture of dust consisting of graphite, silicate, and PAHs, with standard grain properties from Laor & Draine (1993), Li & Draine (2001), and Weingartner & Draine (2001). The input parameters of the model are:

- The metallicity of the star cluster, Z , in units of the solar metallicity Z_\odot (Asplund et al. 2005).
- The age of the star cluster, \mathcal{T} , in Myr.
- The ambient pressure, expressed as

$$p_0 = \log \left(\frac{n_0 T_0}{\text{cm}^{-3} \text{ K}} \right), \quad (11)$$

where n_0 and T_0 are respectively the number density and the temperature of the surrounding ISM.

- The compactness parameter, C , which parametrizes the heating capacity of the star cluster and depends on M_{cl} and p_0 as:

$$C = \frac{3}{5} \log \left(\frac{M_{\text{cl}}}{M_\odot} \right) + \frac{2}{5} p_0. \quad (12)$$

The C parameter determines the dust grain temperature distribution.

- The covering factor, f_{cov} , which represents the fraction of the surface of the H II region covered by the PDR. Note that f_{cov} is the same parameter as the F factor in the model of Popescu et al. (2011). Hereafter the abbreviation f_{cov} will be used to refer to both parameters.

4.3. Observational constraints on the input parameters

The large amount of ancillary data for M33, as well as the results of previous studies from the literature, allowed us to constrain part of the input parameters for both models.

For the model of Popescu et al. (2011) we were able to place the following constraints:

- *Bulge-to-disk ratio*: Using deep H-band ($1.65 \mu\text{m}$) observations of M33, Minniti et al. (1993) found an excess of emission in the innermost $2'$ that they identified with a small bulge. Regan & Vogel (1994) claimed that if a compact bulge is present, it does not make a large contribution to the spheroidal light. More recently, Corbelli & Walterbos (2007) analyzed gas and stellar radial velocities in the innermost 0.5 kpc of M33. Their study showed that the central part of the galaxy does not exhibit kinematic signature of a significant bulge. Since there is no convincing evidence for a bulge in M33, here we opted for a bulge-to-disk ratio (B/D) equal to 0.
- *Inclination angle*: We assumed an inclination angle of 57° based on 21 cm line observations of M33 with the Westerbork Synthesis Radio Telescope (Deul & van der Hulst 1987).
- *B-band scalelength*: We obtained the radial stellar scale length in the B-band, h_s , using the *Sloan g*-band image. The fit of an exponential function to the surface brightness profile gives a value of $h_s=2513 \pm 80 \text{ pc}$ (see Fig. 3). This value

agrees with the scalelength for young star formation tracers such as FUV, NUV and $H\alpha$ (Verley et al. 2009).

- *Dust scalelength*: In the model of Popescu et al. (2011) the scale of the different components are normalised to the B-band scalelength of the disk, h_s . In particular, the Popescu et al. (2011) model assumes that the scalelength of the thick disk of dust (h_d) is a factor 1.4 larger than h_s . To compare the actual geometry of M33 with the model assumptions we calculated the scalelength traced by the SPIRE 500 μm emission. Shorter wavelengths are more affected by the dust temperature distribution, while *Planck* data at longer wavelengths lack the angular resolution necessary to extract isophotal fluxes. For SPIRE 500 μm we found a scalelength of 3200 ± 100 pc (see Fig. 4). If we approximate h_d with this value, we obtain $h_d/h_s = 1.27 \pm 0.08$, close to the value 1.4 assumed in the model.
- *old*: We derived this parameter as 0.05 by assuming that the IRAC 3.6 μm and 4.5 μm bands mainly trace the emission from the old stellar population (Bendo et al. 2015). Then we integrated the luminosity of M33 under these two bands and derived *old* as the ratio of this luminosity and the integrated luminosity of the model galaxy for the old stellar component (Popescu et al. 2011, Tab. E2).

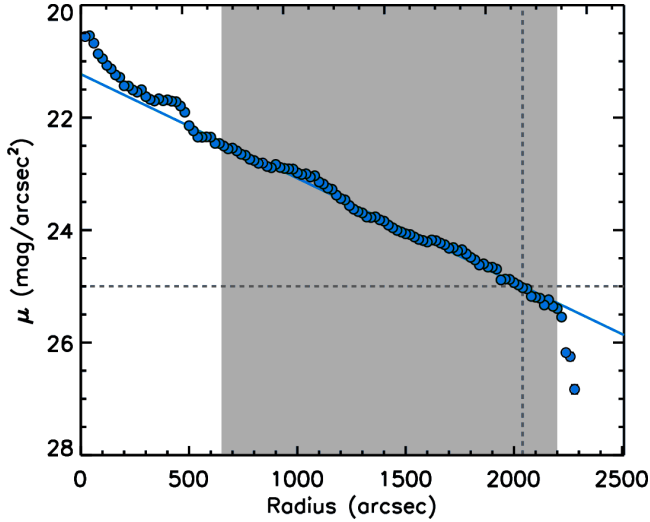


Fig. 3: B-band surface brightness of the stellar disk of M33 plotted against deprojected radius. The background subtracted *Sloan g*-band was used to obtain the average value of circular apertures in the outer parts of M33 disk where previously foreground stars and $H\text{II}$ regions were masked. The fit (solid line) was achieved using the isophotes in the radial range marked by the grey-shaded area. We obtain a final scalelength of 2513 ± 80 pc. The horizontal and vertical dashed gray lines indicate the 25 mag/arcsec² isophote. The error bars are smaller than the data points.

In the case of the model of Groves et al. (2008), we established the following constraints:

- *Metallicity*: Magrini et al. (2007) studied the radial oxygen abundance gradient in M33 using a list of 83 $H\text{II}$ regions with $[\text{O III}] \lambda 4363$ detections. These authors found that $12 + \log[\text{O}/\text{H}]$ ranges from ~ 8.5 to 8.1 (see their Fig. 3). For the solar metallicity presented in Asplund et al. (2005) these limits corresponds to values of Z_\odot from ~ 0.7 to 0.3 . To cover

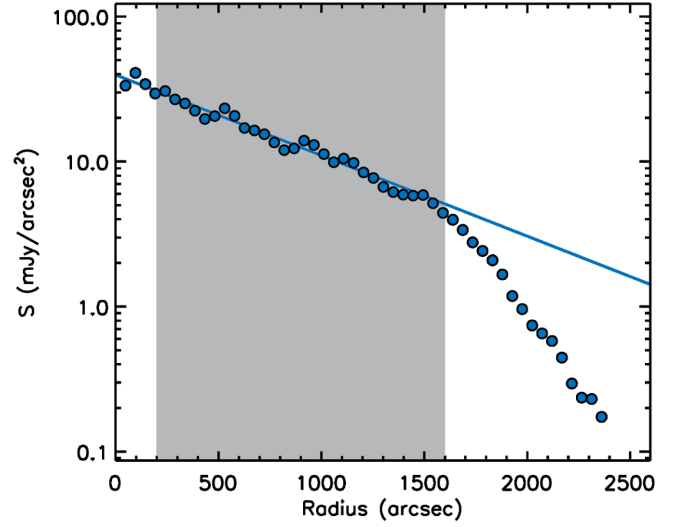


Fig. 4: SPIRE 500 μm surface brightness of M33 plotted against deprojected radius. The fit (solid line) was achieved using the isophotes in the radial range marked by the grey-shaded area. The error bars are smaller than the data points.

this range we constrained the metallicity to the discrete values 1.0, 0.4, and $0.2 Z_\odot$ allowed by the Groves et al. (2008) model.

- *Age*: A small sample of young stellar clusters was studied by Grossi et al. (2010) and Fan & de Grijs (2014), finding that most of the star clusters have ages of ~ 3 Myr. A larger sample was studied by Sharma et al. (2011), who found representative values about 5 Myr in the inner part of disk (galactocentric radii $\lesssim 4$ kpc) and about 7 Myr for star clusters within the outer disk (from 4 to 7 kpc). Therefore, we restricted the age to the range from 3 to 7 Myr.
- *Compactness and ambient pressure*: Unfortunately we could not constrain either C or p_0 , so we left both parameters free in the fitting procedure and checked later if they are within the expected range of values derived from Eq. 12 and the mass range derived by Sharma et al. (2011) for the star clusters in the inner part of M33 (from $10^2 M_\odot$ to $10^5 M_\odot$).

The remaining parameters were left free in the fitting procedure.

4.4. Fitting procedure

In order to find the best-fitting model and its uncertainty for both the SF and the diffuse components we used the following procedure: for each component we generated a total of 100 slightly different data sets by allowing the observed fluxes to randomly vary following a Gaussian distribution within the error bars. For each one of these sets we found the best-fitting model using a χ^2 minimization technique. To build the best-fitting solution (i.e. most probable SED and its range of uncertainty) we extracted the median, the minimum, and the maximum SEDs from the set of 100 best-fitting models. To express the range of values obtained through the iteration process we will use the nomenclature $X_{\text{med}}^{\wedge X_{\text{max}} \vee X_{\text{min}}}$ to report median (X_{med}), maximum (X_{max}), and minimum (X_{min}) values.

5. Results

5.1. Best fit for the SF component

The best-fitting solution for the SF component was obtained by exploring the parameter space of the model of Groves et al. (2008) with the constraints presented in Tab. 3 (see Sect. 4.3 for details). For each one of the 100 iterations, a total of 6885 different parameter combinations were tested to find the minimum χ^2 . Note that *Planck* data could not be used to fit the SF component due to their lack of angular resolution. The best fitting model is shown in Fig. 5, and the range of values found for the parameters is presented in Tab. 3. The reduced χ^2 is $4.69^{+12.15}_{-0.73}$. We found that the metallicity of the best-fitting solution is $0.2^{+0.4}_{-0.2}$, at the low end of the values reported by Magrini et al. (2007).

The best-fitting solution gives a total mass of the stellar clusters of $1.6^{+1.9}_{-0.9} \times 10^6 M_\odot$. Taking into account the number of SF regions detected we can estimate an average value of about $5 \times 10^3 M_\odot$ for the individual stellar clusters, well centered within the limits estimated by Sharma et al. (2011). The dust luminosity associated to the SF regions is $0.42^{+0.49}_{-0.36} \times 10^9 L_\odot$. As Fig. 5 shows, the model of Groves et al. (2008) is not able to reproduce the LABOCA 870 μm observations (see Tab. 4 for details). A complete discussion of this excess is given in Sect. 6.

5.2. Best fit for the diffuse component

We searched the library of the diffuse dust SEDs of Popescu et al. (2011) for the best-fitting solution to the data in the MIR/submm range, leaving τ_B^f and SFR' as free parameters and keeping fixed old to 0.05 and B/D to 0.0 (see Tab. 3 for details). For each one of the 100 iterations we tested a total of 784 different combinations of τ_B^f and SFR' . The flux level was scaled using Eq. 8 and $h_s = 2513$ pc. As we mentioned in Sect. 3, *Planck* data were not used in the fitting procedure since their diffuse fluxes were not directly measured but inferred, while LABOCA 870 μm band was not used due to the observational limitations discussed in Sect. 2.6. The S36mm data point was neither used since the thermal radio continuum is not related to the diffuse ISM but to the ionized gas within the SF component. The results are shown in Fig. 6 and Tab. 4. The reduced χ^2 is $1.82^{+4.44}_{-0.46}$ and the dust luminosity associated to the diffuse component is $1.30^{+1.50}_{-1.08} \times 10^9 L_\odot$.

The model of Popescu et al. (2011) systematically underpredicts the submm and mm estimated fluxes from *Planck* (see Tab. 4 for details). This excess of emission is discussed in Sect. 6.

5.3. Total emission

Once we separately fitted the emission from the SF and the diffuse component, we combined both SEDs to match the global MIR to radio emission of the galaxy, which is shown in Fig. 7. At MIR/FIR wavelengths the observations are reasonably well fitted, while at submm and mm wavelengths the excess of emission found in the individual components translates into a significant excess in the global SED of M33 (Fig. 7), showing up at submm wavelengths and reaching compelling values at mm wavelengths (see Tab. 4). It is important to note that no traces of the excess are visible at the PLANCK 10 mm point extracted from the *Planck* Catalog of Compact Sources (see Sect. 2.7).

From the values that we obtained for the radiation field leaving the SF regions and powering the diffuse dust emission,

Parameter	Abbr.	Units	Range	Value
Metallicity	Z	Z_\odot	0.2-1.0	$0.2^{+0.4}_{-0.2}$
Age	\mathcal{T}	Myr	3.0-7.0	$4.0^{+4.0}_{-3.5}$
Compactness	C	-	Free	$4.0^{+4.0}_{-4.0}$
Ambient pressure	p_0	-	Free	8^{+8}_{-8}
Covering factor	f_{cov}	%	Free	$0.46^{+0.74}_{-0.36}$
Opacity	τ_B^f	-	Free	$2.2^{+2.8}_{-1.6}$
Star formation rate	SFR'	$M_\odot \text{ yr}^{-1}$	Free	$0.25^{+0.29}_{-0.20}$
Old stellar luminosity	old	-	Fixed	0.05
Bulge-to-disk ratio	B/D	-	Fixed	0.0
Inclination angle	i	deg	Fixed	57
B-band scalelength	h_s	pc	Fixed	2513

Table 3: List of the parameters (column 1) with their abbreviations (column 2), units (column 3), and observational constraints (column 4) used to obtain the best-fitting solutions. The median, minimum, and maximum values derived from the fitting procedure are shown in column 5.

SFR' , and for the average fraction of the SF component covered by PDRs, f_{cov} , we estimated the intrinsic SFR of M33 as:

$$SFR = \frac{SFR'}{1 - f_{\text{cov}}} = 0.45^{+1.13}_{-0.31} M_\odot \text{ yr}^{-1}, \quad (13)$$

in good agreement with the value $0.45 \pm 0.10 M_\odot \text{ yr}^{-1}$ found by Verley et al. (2009) using extinction corrected UV and H α measurements.

5.4. Energetic balance

The comparison between the predicted radiation field escaping M33 (see Sect. 4.1 for details) and the observations is shown in Fig. 8. The attenuation and its uncertainty were calculated using $\tau_B^f = 2.2^{+2.8}_{-1.6}$ and $f_{\text{cov}} = 0.46^{+0.74}_{-0.36}$ as explained in Sect. 4.1. The good agreement in the infrared part comes from the fact that the parameter old was scaled by hand to match S_{ν}^{old} to the observations (see Sect. 4.3). On the other hand, in the UV-optical part we found that the integrated luminosity calculated from the observations is $70^{+84}_{-59}\%$ higher than the expected luminosity. This discrepancy is discussed in Sect. 6.

5.5. Gas-to-dust ratio

In the model of Groves et al. (2008), the mass of dust contained in the SF regions depends on the combination of parameters and it scales with M_{cl} . For the SF component of M33 we obtained:

$$M_{\text{dust}}^{\text{SF}} = 2.9^{+3.5}_{-2.5} \times 10^6 M_\odot. \quad (14)$$

The total mass of diffuse dust of M33 can be calculated from the Eq. 44 of Popescu et al. (2011):

$$M_{\text{dust}}^{\text{diff}} = 0.992 \times \tau_B^f \times h_s^2 \text{ pc}^{-2} M_\odot = 13.8^{+17.5}_{-10.0} \times 10^6 M_\odot. \quad (15)$$

Druard et al. (2014) estimated that the total molecular mass of M33 is $0.3 \times 10^9 M_\odot$ using a CO-to-H $_2$ conversion factor

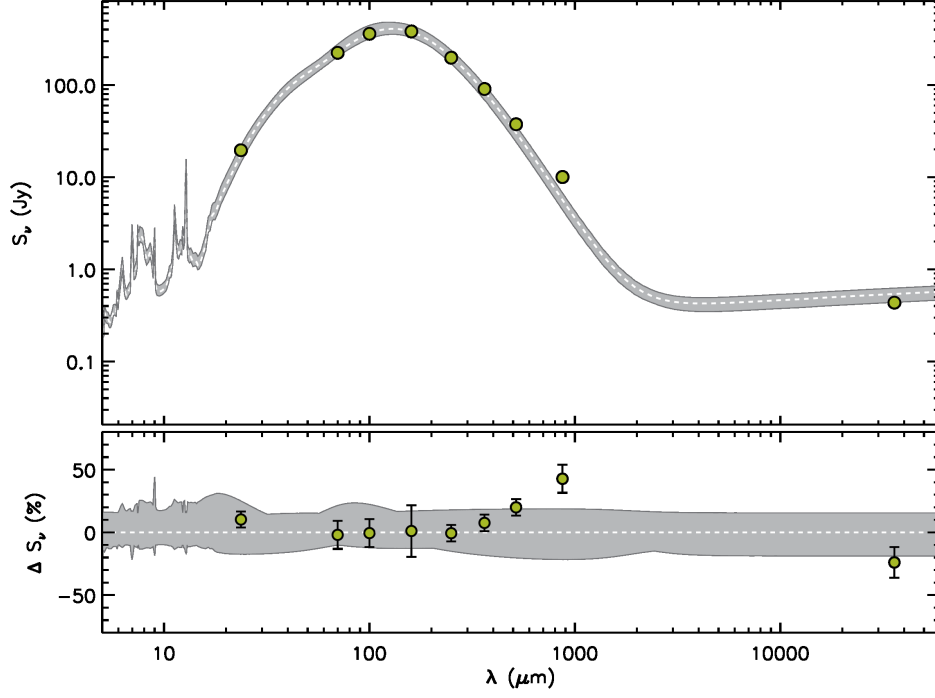


Fig. 5: *Top*: Results of the fitting procedure for the SF component of M33. The green filled circles are the observed fluxes for the SF component presented in Tab. 2. The best-fitting model is represented by the white dashed line while its uncertainty is defined by the gray shaded area. For clarity errors are only shown in the bottom panel. *Bottom*: Residuals of the fitting procedure. The green filled circles corresponds to the percentage difference of the observed fluxes and the best-fitting model (white dashed line). The gray shaded area gives the uncertainty of the best-fitting model in terms of percentage.

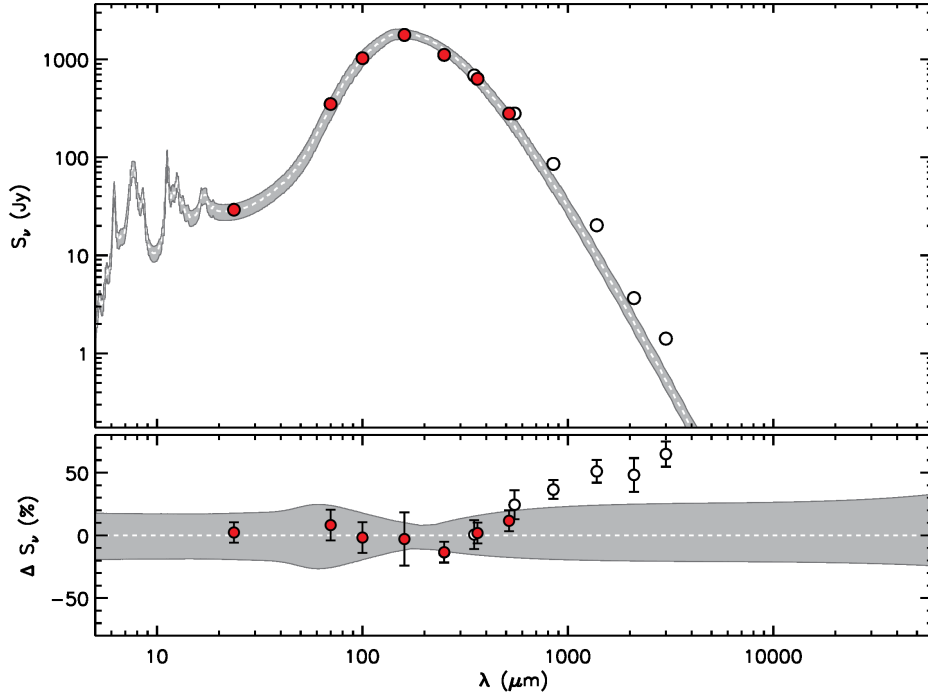


Fig. 6: *Top*: Results of the fitting procedure for the diffuse component of M33. The red filled circles are the observed fluxes for the diffuse component presented in Tab. 2. The best-fitting model is represented by the white dashed line while its uncertainty is defined by the gray shaded area. For clarity errors are only shown in the bottom panel. *Bottom*: Residuals of the fitting procedure. The red filled circles corresponds to the percentage difference of the observed fluxes and the best-fitting model (white dashed line). The gray shaded area gives the uncertainty of the best-fitting model in terms of percentage.

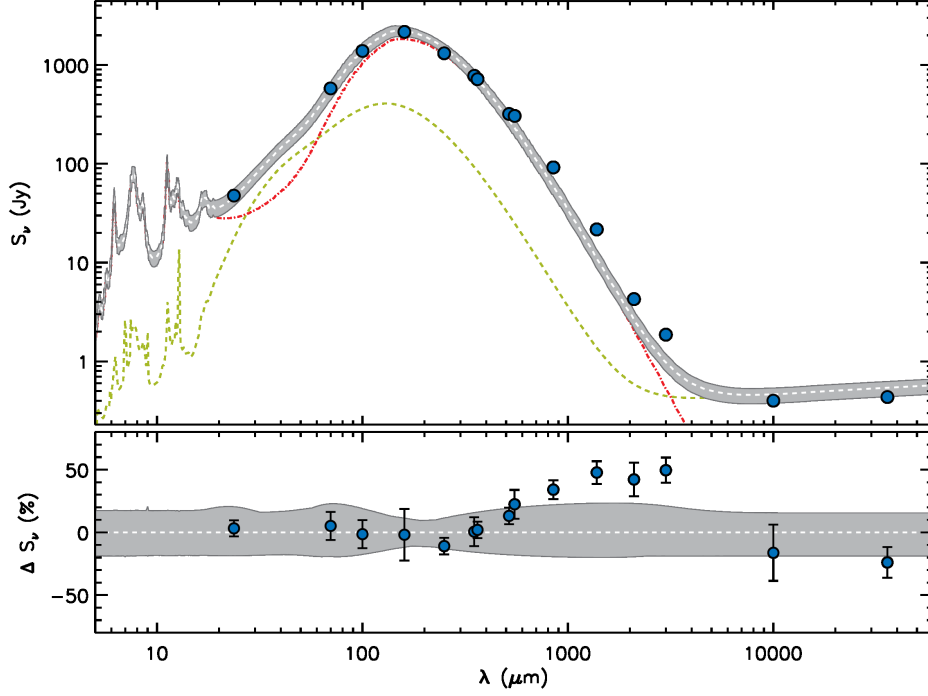


Fig. 7: *Top*: Combination of the best-fitting models for the SF component (green dashed line, see Fig. 5 for details) and the diffuse component (red dashed-dotted line, see Fig. 6 for details). The blue filled circles are the observed fluxes for the entire galaxy presented in Tab. 2. The white dashed line and the gray shaded area correspond to the direct sum of the best-fitting models and their uncertainties obtained for the SF and the diffuse components. For clarity errors are only shown in the bottom panel. *Bottom*: Residuals of the fitting procedure. The blue filled circles corresponds to the percentage difference of the observed fluxes and the best-fitting model (white dashed line). The gray shaded area gives the uncertainty of the best-fitting model in terms of percentage.

$X_{\text{CO}} = N(\text{H}_2)/I_{\text{CO}(1\rightarrow0)} = 4 \times 10^{20} \text{ cm}^{-2}/(\text{K km s}^{-1})$, including helium. Gratier et al. (2010) used Very Large Array (VLA) observations of the atomic gas and derived a total mass of $1.4 \times 10^9 M_\odot$ within a 8.5 kpc radius. From all these values we can derive a gas-to-dust ratio of:

$$G_{\text{dust}} = \frac{M_{\text{atom}} + M_{\text{mol}}}{M_{\text{dust}}^{\text{SF}} + M_{\text{dust}}^{\text{diff}}} = \frac{1.7 \times 10^9 M_\odot}{16.7^{+21.0}_{-12.5} \times 10^6 M_\odot} = 101^{+135}_{-80}, \quad (16)$$

at the low end of the range determined by Kramer et al. (2010), who found, using MBB models, that G_{dust} ranges from 200 to 120 depending on the value of β .

Given the solar value $G_{\text{dust}}=137$ (Draine et al. 2007, Tab. 2), and assuming that the gas-to-dust mass ratio scales linearly with metallicity (i.e., the fraction of metals incorporated in the dust is constant), due to the sub-solar metallicity of M33 we would expect a higher value of G_{dust} between 200 and 450 (see Sect. 4.3 for details). Possible origins for this discrepancy are discussed in Sect. 6.

6. Discussion

Our study has revealed three compelling discrepancies between the models and the observations: excess of emission at submm and mm wavelengths (Fig. 7), deficit of absorption of UV photons (Fig. 8), and abnormally low value of G_{dust} (Sect. 5.5). In the following, we discuss in detail different hypothesis that could explain these discrepancies.

6.1. Cold dust component

A population of very cold dust (VCD) with temperatures below (10 K) has been proposed to explain the excess of emission at submm wavelengths (e.g. Galliano et al. 2003, 2005; Galametz et al. 2009, 2010). Although in general the VCD component is able to fit well the submm excess, this hypotheses is considered unlikely because the large mass of dust required and the strong shielding from the ambient radiation field necessary to keep the grains at such low temperatures (Lisenfeld et al. 2002). In this line, Galliano et al. (2011) found that the submm excess in the LMC can not be produced by a cold dust component.

To explore the VCD hypothesis in the case of M33 we added to its total SED a MBB component with $\beta=2$ (see top panel of Fig. 9). We found that the submm and mm excess can be well fitted using a temperature of ~ 6 K. The mass of dust required to produce such emission is:

$$M_{\text{VCD}} \sim 40 \times 10^6 M_\odot, \quad (17)$$

which is about three times higher than the combined mass of dust found in the SF and the diffuse components. Adding this extra mass of dust would imply an unreasonably low value of $G_{\text{dust}} \lesssim 50$. For reference, note that Baes et al. (2014) found a value $G_{\text{dust}} < 14.5$ for the extreme case of NGC 5485, an early type galaxy with no atomic or molecular gas detected but with a prominent dust lane perpendicular to the photometric major axis.

BAND	$\frac{S_{\text{SF}}^{\text{obs}}}{S_{\text{SF}}^{\text{mod}}}$	$\frac{\Delta_{\text{SF}}}{\sqrt{(\delta_{\text{SF}}^{\text{obs}})^2 + (\delta_{\text{SF}}^{\text{mod}})^2}}$	$\frac{S_{\text{DIFF}}^{\text{obs}}}{S_{\text{DIFF}}^{\text{mod}}}$	$\frac{\Delta_{\text{DIFF}}}{\sqrt{(\delta_{\text{DIFF}}^{\text{obs}})^2 + (\delta_{\text{DIFF}}^{\text{mod}})^2}}$	$\frac{S_{\text{TOT}}^{\text{obs}}}{S_{\text{TOT}}^{\text{mod}}}$	$\frac{\Delta_{\text{TOT}}}{\sqrt{(\delta_{\text{TOT}}^{\text{obs}})^2 + (\delta_{\text{TOT}}^{\text{mod}})^2}}$
GALEX FUV	-	-	-	-	$4.28^{+197.88}_{-2.64}$	5.22
GALEX NUV	-	-	-	-	$3.98^{+8.18}_{-2.91}$	7.76
Sloan u-band	-	-	-	-	$1.68^{+2.35}_{-1.35}$	2.70
MIPS 24 μm	$1.11^{+1.35}_{-0.89}$	0.44	$1.02^{+1.27}_{-0.87}$	0.12	$1.03^{+1.27}_{-0.86}$	0.17
PACS 70 μm	$0.98^{+1.09}_{-0.81}$	-0.13	$1.09^{+1.47}_{-0.88}$	0.33	$1.05^{+1.30}_{-0.86}$	0.24
PACS 100 μm	$0.99^{+1.13}_{-0.81}$	-0.03	$0.98^{+1.22}_{-0.84}$	-0.07	$0.99^{+1.20}_{-0.83}$	-0.07
PACS 160 μm	$1.01^{+1.16}_{-0.86}$	0.04	$0.97^{+1.10}_{-0.88}$	-0.12	$0.98^{+1.11}_{-0.88}$	-0.08
SPIRE 250 μm	$0.99^{+1.17}_{-0.84}$	-0.04	$0.88^{+1.01}_{-0.80}$	-0.78	$0.90^{+1.04}_{-0.81}$	-0.68
PLANCK 350 μm	-	-	$1.01^{+1.19}_{-0.87}$	0.03	$1.01^{+1.19}_{-0.87}$	0.03
SPIRE 350 μm	$1.08^{+1.32}_{-0.91}$	0.42	$1.02^{+1.21}_{-0.88}$	0.11	$1.02^{+1.21}_{-0.88}$	0.12
SPIRE 500 μm	$1.25^{+1.57}_{-1.05}$	1.26	$1.13^{+1.37}_{-0.95}$	0.63	$1.15^{+1.40}_{-0.97}$	0.74
PLANCK 550 μm	-	-	$1.32^{+1.61}_{-1.11}$	1.41	$1.29^{+1.57}_{-1.08}$	1.27
PLANCK 850 μm	-	-	$1.58^{+1.95}_{-1.29}$	2.45	$1.52^{+1.88}_{-1.24}$	2.23
LABOCA 870 μm	$1.75^{+2.23}_{-1.47}$	3.43	-	-	-	-
PLANCK 1.4 mm	-	-	$2.04^{+2.55}_{-1.65}$	4.07	$1.91^{+2.39}_{-1.55}$	3.66
PLANCK 2.1 mm	-	-	$1.93^{+2.43}_{-1.55}$	3.29	$1.73^{+2.15}_{-1.41}$	2.74
PLANCK 3.0 mm	-	-	$2.84^{+3.58}_{-2.27}$	6.78	$1.98^{+2.44}_{-1.64}$	4.24
PLANCK 10 mm	-	-	-	-	$0.86^{+1.06}_{-0.74}$	-0.48
S 36 mm	$0.81^{+0.99}_{-0.70}$	-0.86	-	-	$0.81^{+0.99}_{-0.70}$	-0.86

Table 4: Comparison of the observations and the models for the SF component (columns 2 and 3), the diffuse component (columns 4 and 5), and the total emission (columns 6 and 7) for M33. In the three cases Δ gives the deviation of the observed data points from the model expectations, while δ^{obs} and δ^{mod} corresponds to the relative error of the observations and the models, respectively.

6.2. Spinning grains

Draine & Lazarian (1998) proposed that electric dipole radiation from spinning grains are responsible for the anomalous emission of the diffuse Galactic background peaking near 10 mm. In the Draine & Lazarian (1998) model the very small grains are disk-like shaped while large grains are spherical, and both rotate around their axis of major inertia, which produces that the frequency of photons emitted is identical to the angular frequency. According to these authors, the rotational excitation of the spinning grains is dominated by collisions with ions and plasma drag and the rotation rate depends on several factors such as the intensity of the radiation field and the physical parameters of the gas phase. For example, while the peak of the emission from spinning grains ranges from ~ 7 to 15 mm in the cold neutral, warm neutral and warm ionized medium, it can reach values below 2 mm in PDRs (see Hoang et al. 2010 for a refined version of the model of Draine & Lazarian 1998).

To study the possibility of spinning dust grains as responsible for the excess of emission detected in M33 we included their contribution in the total SED. As the mid panel of Fig. 9 shows, the excess of emission at wavelengths $\lesssim 2$ mm can not be reproduced even if we assume spinning grains rotating at the highest rate allowed by Hoang et al. (2010). Moreover, the contribution from spinning grains degrade the good agreement pre-

viously found between models and observations at wavelengths around 10 mm.

6.3. Magnetic nanoparticles

Draine & Hensley (2013) claimed that if part of the interstellar Fe forms ferro- or ferri-magnetic grains, then the magnetic dipole radiation from these grains might contribute significantly to the total dust SED. These authors considered three materials as potential candidates: metallic Fe, magnetite (Fe_3O_4), and maghemite ($\gamma\text{-Fe}_2\text{O}_3$). Draine & Hensley (2012) show how magnetic grains are able to explain the strong excess of submm and mm emission found in the SMC.

In order to test if magnetic nanoparticles can explain the excess of emission found in M33 we fitted the SED expected for 10 nm metallic Fe grains at 18 K (see right panel in Fig. 8 of Draine & Hensley 2013) by adjusting the intensity until the best fit to the FIR-mm data points was achieved, as it is shown in the bottom panel of Fig. 9. The contribution from magnetic grains can alleviate the mm and submm excess but is not able to satisfactory fit the data in this wavelength range. In addition, the fit at the PLANCK 10 mm. We also tested the possibility of 100 nm metallic Fe grains at 18 K. The fit is worse than for the 10 nm grains in the submm/mm/PLANCK 10 mm range. In addition, they have a strong impact on the peak of the SED thus degrading

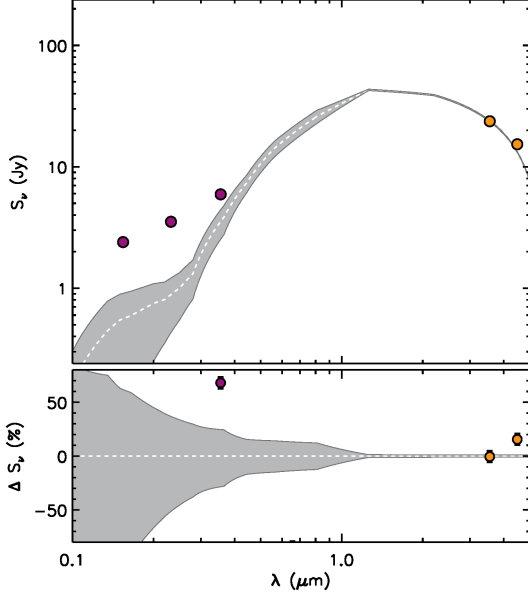


Fig. 8: *Top*: Results of the fitting procedure for the stellar component of M33. The purple and orange filled circles are respectively the observed fluxes of the young and the old stellar populations presented in Tab. 2. The white dashed line and the gray shaded area correspond to the combination of the attenuated emission and uncertainty of the young and old stellar populations ($S_{v,young}$ and $S_{v,old}$, respectively). For clarity errors are only shown in the bottom panel. *Bottom*: Residuals of the fitting procedure. The filled circles corresponds to the percentage difference of the observed fluxes and the best-fitting model (white dashed line). The gray shaded area gives the uncertainty of the best-fitting model in terms of percentage.

the fit at wavelengths $\sim 150\mu\text{m}$. Thus, for M33, in contrast to the SMC, magnetic grain emission is not an entirely satisfactory explanation for the mm and submm excess.

6.4. CO-to- H_2 conversion factor

The low value of G_{dust} obtained here depends in part on the mass of molecular gas obtained by Druard et al. (2014), who determined a conversion factor $X_{\text{CO}} = 4 \times 10^{20} \text{ cm}^{-2}/(\text{K km s}^{-1})$ for M33, about twice higher than the Galactic value which is reasonable for the ~ 2 times lower metallicity. A value of $X_{\text{CO}} \gtrsim 20 \times 10^{20} \text{ cm}^{-2}/(\text{K km s}^{-1})$ would provide enough molecular gas to achieve a G_{dust} in the expected range of $G_{\text{dust}} \gtrsim 200$. However, this is a unreasonably high value for the case of M33, where combining CO, H I, and IR measurements, Leroy et al. (2011) did not find evidence of such deviations in the value of X_{CO} .

6.5. Porosity

A porous ISM would allow a higher fraction of the UV radiation to escape the galaxy without interacting with the dust thus alleviating the UV discrepancy. Several theoretical studies try to explain how the internal properties of galaxies affect the escape fraction. Among the properties that can influence the escape fraction are: the covering factor of the clumps in the ISM, as well as the density of the clumped and inter clump medium

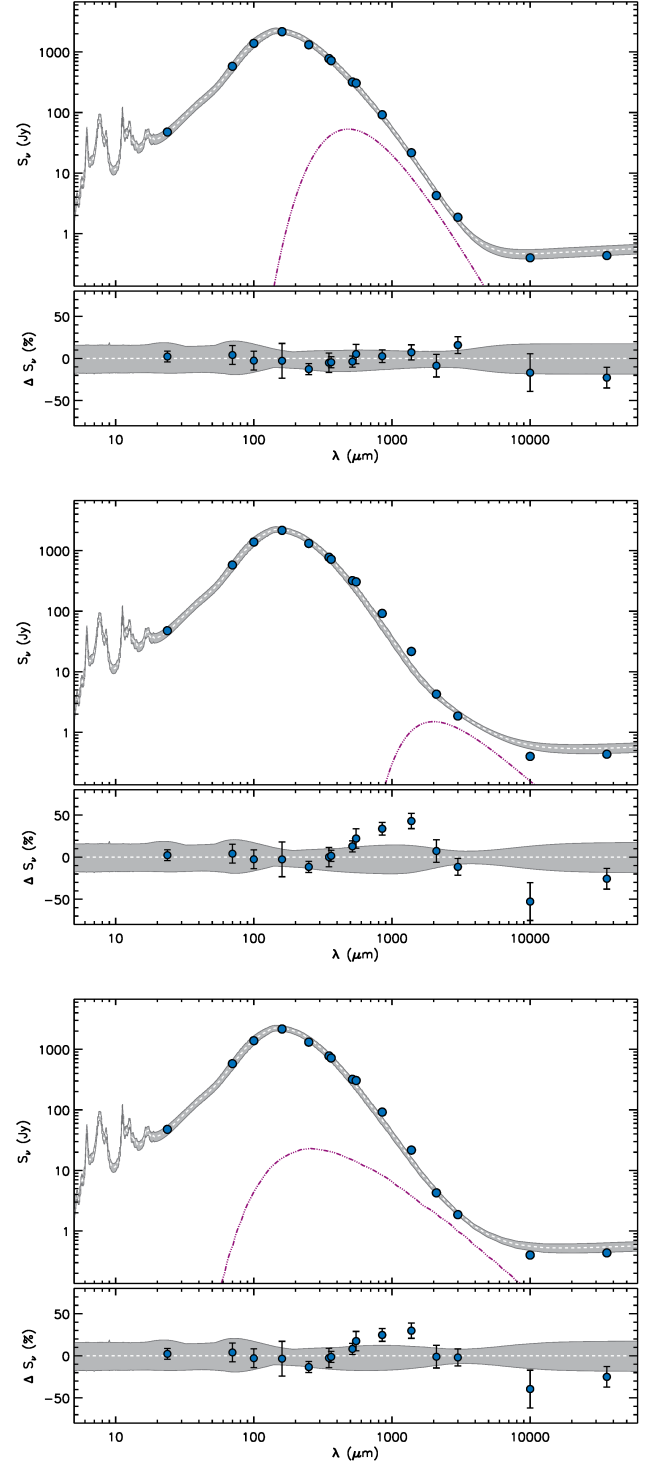


Fig. 9: Total SED of M33 (see Fig. 7 for a detailed description) combined with an extra component (purple line-dashed) to account for the emission from very cold dust (top panel), spinning dust grains (mid panel), and magnetic nanoparticles (bottom panel).

(Fernandez & Shull 2011), blow-out of shells created by supernova (SN) remnants that provide the photons with a clear path to escape the galaxy (Dove & Shull 1994), and the porosity of the ISM given as the fraction of the ISM that is devoid of H I owing to the expansion of SN-driven bubbles. Therefore, the UV dis-

crepancy derived from our modeling might be due to large shell structures across the whole galactic disk (Relaño et al. 2013).

6.6. Dust heated by evolved stars

Could an unrealistic SED of the stellar populations that are heating the dust be responsible for the mm and submm excess and/or the UV discrepancy? Popescu et al. (2011) discussed in detail the influence of the spectral shape of the stellar radiation on the dust SED (see their Sect. 4.3). They concluded that the stellar SED does not affect significantly the shape of the dust SED and that the most relevant parameters shaping the dust SED are the overall stellar luminosities as well as the geometry and the properties of the dust. Therefore, the exact shape of the stellar SED is unlikely to be a very important source of error in our study.

In order to quantify in M33 the contribution to the dust heating by the evolved stellar population, we set SFR to 0 and checked the amplitude of the diffuse SED keeping the remaining values the same as in our best-fitting solution. We found that this contribution is indeed negligible with the exception of the wavelengths around the peak, where it contributes slightly to the dust emission. It is noteworthy that this result is at first sight in contradiction with the results of Boquien et al. (2011), who found a tight correlation between the 250/350 μm ratio and the 3.6 μm luminosity ($L_{3.6\mu\text{m}}$) at scales of 42'' (~ 170 pc) that they interpret as an indication of the old stars being the main heating source of the dust emitting in the 250–350 μm wavelength range. This apparent discrepancy between our study and Boquien et al. (2011) is not real but it comes from different definitions of what is considered “old” stellar population (see our Sect. 4.1 for details).

6.7. Geometry

The discrepancies revealed by our study might be explained by differences between the actual geometry of M33 and the geometry assumed by the model of Popescu et al. (2011, Tab. E.1). As we mentioned in Sect. 4.3, there is no evidence of any discrepancy regarding the radial dimensions of the disk of dust. Regarding the vertical dimensions, for a B-band scalelength of 2513 pc, the model of Popescu et al. (2011) predicts scaleheights of 186 pc for the old stellar disk, 121 pc for the thick disk of dust, and 40 pc for both the young stellar disk and the thin disk of dust. Using the break of the power-spectrum in different emission bands, Combes et al. (2012) were able to give an estimation of the thickness of the stellar and dust disks of M33: cold dust lies in a 350 pc disk, warm dust lies in a 100 pc disk, and the thickness of the stellar disk in the FUV and NUV bands was found to be 40 pc and 56 pc, respectively. Unfortunately, the conversion of the breaks found by Combes et al. (2012) to scaleheights is not straightforward since it depends on the conditions in the disk as the simulations of Combes et al. (2012, Tab. 4) have shown. Therefore, we can not exclude that the discrepancies found in our study are due to differences between the vertical dimensions of M33 and the model assumptions.

6.8. Different dust properties

Differences between the actual dust properties of the low metallicity galaxy M33 and those adopted in the models (Laor & Draine 1993; Li & Draine 2001; Weingartner & Draine 2001; Draine & Li 2007) might explain simultaneously the three discrepancies found. Recently Jones et al. (2013) proposed that

interstellar dust in the diffuse ISM might be characterized by a lower emissivity index β at long wavelengths. If this is the case, these dust grains would provide flatter emission at submm and mm wavelengths, which would result in a better agreement between our modeling and the observations. Additionally, a lower emissivity index resulting in a higher extinction coefficient would allow a lower dust surface density to account for the dust emission, which would result in a decrement of the UV absorption, and thus a lower UV excess, and a lower dust mass, thus increasing the value of G_{dust} .

7. Summary and conclusions

We have modeled separately the emission coming from the SF regions and from the diffuse ISM in the spiral galaxy M33, using radiation transfer models based on dust grains with standard properties. Thanks to the wide set of data available for this galaxy, as well as the numerous previous studies from other authors, we could constrain an important part of the parameters used by the models.

For the SF component, we found that the model of Groves et al. (2008) is able to reproduce the MIR-FIR observations and the thermal radio continuum. However, we found that the model underestimates the LABOCA data and it is barely compatible with the SPIRE 500 μm data. Regarding the diffuse component, we found that the model of Popescu et al. (2011) fits well the MIR/FIR data points but underpredicts severely the observations longwards 800 μm . We also found that our modeling underpredicts by $70^{+84}_{-59}\%$ the UV radiation that escapes the galaxy without interacting with the dust. We derived a gas-to-dust ratio $G_{\text{dust}} = 101^{+135}_{-80}$, significantly lower than the expected value based on the sub-solar metallicity of M33.

We discussed various processes that could explain these discrepancies. A cold dust component emitting in the submm and mm is unlikely due to the large mass of dust that would be needed. Spinning grains and the magnetic nanoparticles can not reproduce well the submm and mm excess and they seriously degrade the fit at other wavelengths. Previous studies of the molecular gas in M33 discards the possibility of anomalies in the X_{CO} conversion factor that could explain the low value of G_{dust} . Since in the model of Popescu et al. (2011) the exact shape of the stellar radiation field has little influence in the dust emission, dust heating from evolved stars is unlikely to be a source of error. Differences in the geometry assumed by the model and the actual geometry of M33 could explain the discrepancies but there is no observational evidence for such differences. A porous ISM could explain to the excess escape of UV radiation.

As a final option, we discussed different physical properties of the dust grains. A lower β would flatten the dust emission at submm and mm wavelengths, decrease the UV attenuation, and bring the gas-to-dust ratio closer to the expected value, thus explaining simultaneously the three discrepancies.

Acknowledgements. We thank the second referee for her/his constructive report and helpful suggestions. We thank F.-X. Désert for his invaluable help with *Planck* data. This work was partially supported by a Junta de Andalucía Grant FQM108, a Spanish MEC Grant AYA-2011-24728 and AYA2014-53506-P, Juan de la Cierva fellowship Program and the European Reintegration Grant ERG HER-SFR. TRL thanks the support of the Spanish Ministerio de Educación, Cultura y Deporte by means of the FPU fellowship. MA acknowledges support by the German Research Foundation (DFG) in the framework of the priority program 1573, “Physics of the Interstellar Medium”, through grant number AL 1467/2-1. This research made use of the NASA/IPAC Extragalactic Database (NED), which is operated by the Jet Propulsion Laboratory, California Institute of Technology, under contract with the National Aeronautics and Space Administration. We also acknowledge the use of the HyperLeda

database (<http://leda.univ-lyon1.fr>). Funding for the creation and distribution of the SDSS Archive has been provided by the Alfred P. Sloan Foundation, the Participating Institutions, the National Aeronautics and Space Administration, the National Science Foundation, the US Department of Energy, the Japanese Monbukagakusho, and the Max Planck Society. The SDSS Web site is <http://www.sdss.org/>. The SDSS is managed by the Astrophysical Research Consortium (ARC) for the Participating Institutions. The Participating Institutions are The University of Chicago, Fermilab, the Institute for Advanced Study, the Japan Participation Group, The Johns Hopkins University, the Korean Scientist Group, Los Alamos National Laboratory, the Max-Planck-Institute for Astronomy (MPIA), the Max-Planck-Institute for Astrophysics (MPA), New Mexico State University, University of Pittsburgh, University of Portsmouth, Princeton University, the United States Naval Observatory, and the University of Washington. This research made use of Montage, funded by the National Aeronautics and Space Administration's Earth Science Technology Office, Computational Technologies Project, under Cooperative Agreement Number NCC5-626 between NASA and the California Institute of Technology. The code is maintained by the NASA/IPAC Infrared Science Archive. This research made use of python (<http://www.python.org>), of Matplotlib (Hunter 2007), a suite of open-source python modules that provides a framework for creating scientific plots, and Astropy, a community-developed core Python package for Astronomy (Astropy Collaboration et al. 2013). This research made use of APLpy, an open-source plotting package for Python hosted at <http://aplpy.github.com>.

References

- Abazajian, K. N., Adelman-McCarthy, J. K., Agüeros, M. A., et al. 2009, *ApJS*, 182, 543
- Ade, P. A. R., Aghanim, N., Arnaud, M., et al. 2014, *ArXiv e-prints*
- Aniano, G., Draine, B. T., Gordon, K. D., & Sandstrom, K. 2011, *PASP*, 123, 1218
- Asplund, M., Grevesse, N., & Sauval, A. J. 2005, in *Astronomical Society of the Pacific Conference Series*, Vol. 336, *Cosmic Abundances as Records of Stellar Evolution and Nucleosynthesis*, ed. T. G. Barnes, III & F. N. Bash, 25
- Astropy Collaboration, Robitaille, T. P., Tollerud, E. J., et al. 2013, *A&A*, 558, A33
- Baes, M., Allaert, F., Sarzi, M., et al. 2014, *MNRAS*, 444, L90
- Bendo, G. J., Baes, M., Bianchi, S., et al. 2015, *MNRAS*, 448, 135
- Bendo, G. J., Buckalew, B. A., Dale, D. A., et al. 2006, *ApJ*, 645, 134
- Bendo, G. J., Griffin, M. J., Bock, J. J., et al. 2013, *MNRAS*, 433, 3062
- Bertin, E. & Arnouts, S. 1996, *A&AS*, 117, 393
- Boquien, M., Calzetti, D., Aalto, S., et al. 2015, *ArXiv e-prints*
- Boquien, M., Calzetti, D., Combes, F., et al. 2011, *AJ*, 142, 111
- Boquien, M., Calzetti, D., Kramer, C., et al. 2010, *A&A*, 518, L70
- Bot, C., Ysard, N., Paradis, D., et al. 2010, *A&A*, 523, A20
- Braine, J., Gratier, P., Kramer, C., et al. 2010, *A&A*, 520, A107
- Combes, F., Boquien, M., Kramer, C., et al. 2012, *A&A*, 539, A67
- Corbelli, E. & Walterbos, R. A. M. 2007, *ApJ*, 669, 315
- Dale, D. A., Aniano, G., Engelbracht, C. W., et al. 2012, *ApJ*, 745, 95
- Deul, E. R. & van der Hulst, J. M. 1987, *A&AS*, 67, 509
- Dove, J. B. & Shull, J. M. 1994, *ApJ*, 430, 222
- Draine, B. T., Dale, D. A., Bendo, G., et al. 2007, *ApJ*, 663, 866
- Draine, B. T. & Hensley, B. 2012, *ApJ*, 757, 103
- Draine, B. T. & Hensley, B. 2013, *ApJ*, 765, 159
- Draine, B. T. & Lazarian, A. 1998, *ApJ*, 508, 157
- Draine, B. T. & Li, A. 2007, *ApJ*, 657, 810
- Druard, C., Braine, J., Schuster, K. F., et al. 2014, *A&A*, 567, A118
- Engelbracht, C. W., Blaylock, M., Su, K. Y. L., et al. 2007, *PASP*, 119, 994
- Ercolano, B., Barlow, M. J., & Storey, P. J. 2005, *MNRAS*, 362, 1038
- Fan, Z. & de Grijs, R. 2014, *ApJS*, 211, 22
- Fazio, G. G., Hora, J. L., Allen, L. E., et al. 2004, *ApJS*, 154, 10
- Fernandez, E. R. & Shull, J. M. 2011, *ApJ*, 731, 20
- Freedman, W. L., Wilson, C. D., & Madore, B. F. 1991, *ApJ*, 372, 455
- Galametz, M., Albrecht, M., Kennicutt, R., et al. 2014, *MNRAS*, 439, 2542
- Galametz, M., Madden, S., Galliano, F., et al. 2009, *A&A*, 508, 645
- Galametz, M., Madden, S. C., Galliano, F., et al. 2011, *A&A*, 532, A56
- Galametz, M., Madden, S. C., Galliano, F., et al. 2010, *A&A*, 518, L55
- Galliano, F., Hony, S., Bernard, J.-P., et al. 2011, *A&A*, 536, A88
- Galliano, F., Madden, S. C., Jones, A. P., Wilson, C. D., & Bernard, J.-P. 2005, *A&A*, 434, 867
- Galliano, F., Madden, S. C., Jones, A. P., et al. 2003, *A&A*, 407, 159
- Gil de Paz, A., Boissier, S., Madore, B. F., et al. 2007, *ApJS*, 173, 185
- Gordon, K. D., Roman-Duval, J., Bot, C., et al. 2014, *ApJ*, 797, 85
- Górski, K. M., Hivon, E., Banday, A. J., et al. 2005, *ApJ*, 622, 759
- Gratier, P., Braine, J., Rodríguez-Fernández, N. J., et al. 2010, *A&A*, 522, A3
- Greenawalt, B. E. 1998, PhD thesis, NEW MEXICO STATE UNIVERSITY
- Griffin, M. J., Abergel, A., Abreu, A., et al. 2010, *A&A*, 518, L3
- Grossi, M., Corbelli, E., Giovanardi, C., & Magrini, L. 2010, *A&A*, 521, A41
- Groves, B., Dopita, M. A., Sutherland, R. S., et al. 2008, *ApJS*, 176, 438
- Güsten, R., Nyman, L. Å., Schilke, P., et al. 2006, *A&A*, 454, L13
- Hermelo, I., Lisenfeld, U., Relaño, M., et al. 2013, *A&A*, 549, A70
- Hipplein, H., Haas, M., Tuffs, R. J., et al. 2003, *A&A*, 407, 137
- Hoang, T., Draine, B. T., & Lazarian, A. 2010, *ApJ*, 715, 1462
- Hoopes, C. G. & Walterbos, R. A. M. 2000, *ApJ*, 541, 597
- Hunter, J. D. 2007, *Computing In Science & Engineering*, 9, 90
- Israel, F. P., Wall, W. F., Raban, D., et al. 2010, *A&A*, 519, A67
- Jones, A. P., Fanciullo, L., Köhler, M., et al. 2013, *A&A*, 558, A62
- Kirkpatrick, A., Calzetti, D., Galametz, M., et al. 2013, *ApJ*, 778, 51
- Kramer, C., Buchbender, C., Xilouris, E. M., et al. 2010, *A&A*, 518, L67
- Laor, A. & Draine, B. T. 1993, *ApJ*, 402, 441
- Leroy, A. K., Bolatto, A., Gordon, K., et al. 2011, *ApJ*, 737, 12
- Li, A. & Draine, B. T. 2001, *ApJ*, 554, 778
- Lisenfeld, U., Israel, F. P., Stil, J. M., & Sievers, A. 2002, *A&A*, 382, 860
- Magrini, L., Vilchez, J. M., Mampaso, A., Corradi, R. L. M., & Leisy, P. 2007, *A&A*, 470, 865
- Makovoz, D. & Marleau, F. R. 2005, *PASP*, 117, 1113
- Martin, D. C., Fanion, J., Schiminovich, D., et al. 2005, *ApJ*, 619, L1
- Minniti, D., Olszewski, E. W., & Rieke, M. 1993, *ApJ*, 410, L79
- Morrissey, P., Conrow, T., Barlow, T. A., et al. 2007, *ApJS*, 173, 682
- Ott, S. 2010, in *Astronomical Society of the Pacific Conference Series*, Vol. 434, *Astronomical Data Analysis Software and Systems XIX*, ed. Y. Mizumoto, K.-I. Morita, & M. Ohishi, 139
- Ott, S. 2011, in *Astronomical Society of the Pacific Conference Series*, Vol. 442, *Astronomical Data Analysis Software and Systems XX*, ed. I. N. Evans, A. Accomazzi, D. J. Mink, & A. H. Rots, 347
- Padmanabhan, N., Schlegel, D. J., Finkbeiner, D. P., et al. 2008, *ApJ*, 674, 1217
- Paradis, D., Paladini, R., Noriega-Crespo, A., et al. 2011, *ApJ*, 735, 6
- Planck Collaboration. 2011, *A&A*, 536, A17
- Planck Collaboration, Ade, P. A. R., Aghanim, N., et al. 2014a, *A&A*, 571, A1
- Planck Collaboration, Ade, P. A. R., Aghanim, N., et al. 2014b, *A&A*, 571, A13
- Planck Collaboration, Ade, P. A. R., Aghanim, N., et al. 2014c, *A&A*, 571, A28
- Planck Collaboration, Ade, P. A. R., Aghanim, N., et al. 2014d, *A&A*, 571, A9
- Planck Collaboration, Ade, P. A. R., Aghanim, N., et al. 2014e, *A&A*, 571, A12
- Poglitsch, A., Waelkens, C., Geis, N., et al. 2010, *A&A*, 518, L2
- Popescu, C. C., Tuffs, R. J., Dopita, M. A., et al. 2011, *A&A*, 527, A109
- Reach, W. T., Megeath, S. T., Cohen, M., et al. 2005, *PASP*, 117, 978
- Regan, M. W. & Vogel, S. N. 1994, *ApJ*, 434, 536
- Relaño, M., Verley, S., Pérez, I., et al. 2013, *A&A*, 552, A140
- Rieke, G. H., Young, E. T., Engelbracht, C. W., et al. 2004, *ApJS*, 154, 25
- Roussel, H. 2013, *PASP*, 125, 1126
- Rowan-Robinson, M., Babbidge, T., Oliver, S., et al. 2008, *MNRAS*, 386, 697
- Schuller, F., Menten, K. M., Contreras, Y., et al. 2009, *A&A*, 504, 415
- Schuster, K.-F., Boucher, C., Brunswig, W., et al. 2004, *ApJ*, 619, L171
- Serra Díaz-Cano, L. & Jones, A. P. 2008, *A&A*, 492, 127
- Sharma, S., Corbelli, E., Giovanardi, C., Hunt, L. K., & Palla, F. 2011, *A&A*, 534, A96
- Siringo, G., Kreysa, E., Kovács, A., et al. 2009, *A&A*, 497, 945
- Tabatabaei, F. S., Beck, R., Krügel, E., et al. 2007a, *A&A*, 475, 133
- Tabatabaei, F. S., Braine, J., Xilouris, E. M., et al. 2014, *A&A*, 561, A95
- Tabatabaei, F. S., Krause, M., & Beck, R. 2007b, *A&A*, 472, 785
- Thilker, D. A., Hoopes, C. G., Bianchi, L., et al. 2005, *ApJ*, 619, L67
- Tuffs, R. J., Popescu, C. C., Völk, H. J., Kylafis, N. D., & Dopita, M. A. 2004, *A&A*, 419, 821
- Verley, S., Corbelli, E., Giovanardi, C., & Hunt, L. K. 2009, *A&A*, 493, 453
- Verley, S., Corbelli, E., Giovanardi, C., & Hunt, L. K. 2010a, *A&A*, 510, A64
- Verley, S., Hunt, L. K., Corbelli, E., & Giovanardi, C. 2007, *A&A*, 476, 1161
- Verley, S., Relaño, M., Kramer, C., et al. 2010b, *A&A*, 518, L68
- Weingartner, J. C. & Draine, B. T. 2001, *ApJ*, 548, 296
- Werner, M. W., Roellig, T. L., Low, F. J., et al. 2004, *ApJS*, 154, 1
- Xilouris, E. M., Tabatabaei, F. S., Boquien, M., et al. 2012, *A&A*, 543, A74
- York, D. G., Adelman, J., Anderson, Jr., J. E., et al. 2000, *AJ*, 120, 1579

Appendix A: MBB fit and color corrections

As pointed out in Sect. 1, MBB models are one of the simplest and widely used techniques to fit the dust SED. Kramer et al. (2010) found that a MBB with $\beta=1.5$ can reproduce the dust SED of M33 up to of $500\mu\text{m}$, the longest wavelength available in their study. Here we confirm that the value $\beta=1.5$ found by these authors is still valid up to wavelengths of 3 mm as revealed by *Planck* data (see Fig. A.1).

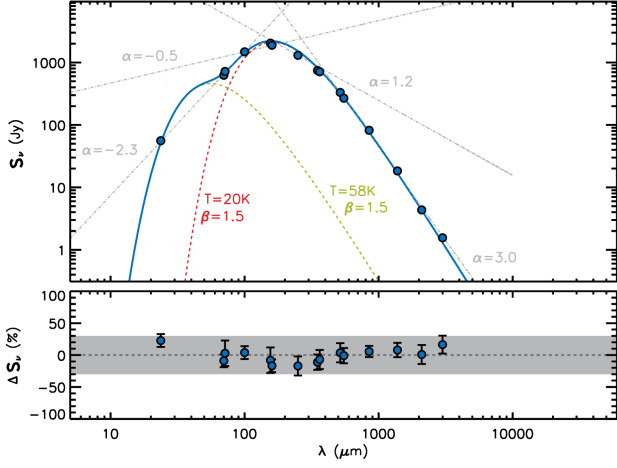


Fig. A.1: Characterization of the SED of M33 using MBB and power-law spectra. The residuals shown in the bottom panel correspond to the MBB fit. The gray shaded area of $\pm 30\%$ is included to facilitate the reading.

As we mentioned in Sect. 3, our photometric measurements were color corrected. Color corrections are necessary to compare monochromatic fluxes with the models of Popescu et al. (2011) and Groves et al. (2008). In order to select appropriate SED profiles in the immediacy of each data point, we mimicked the observations of M33 using MBB models and power-laws, $S_\nu \propto \nu^\alpha$.

We found that the observations of M33 can be well reproduced with both a two-component modified black body of $\beta=1.5$ and $T=20$ K and $T=57$ K or a combination of four power-laws with indices ranging from -2.3 to 3.0 (see Fig. A.1 for details). Then we searched in the tables for MIPS⁷, PACS⁸, SPIRE⁹, and *Planck* (Planck Collaboration et al. 2014d) for the listed color corrections that best correspond to the profiles found. For example, for MIPS $24\mu\text{m}$ we used the value 0.960 tabulated for a power-law of index -2.0 (no values are listed for -2.3). For the remaining PACS, and SPIRE bands we found lower corrections. In the case of *Planck* data, color corrections are higher, with values ranging from 0.963 at 143 GHz to 0.854 at 545 GHz.

Appendix B: CMB subtraction

The angular size of the fluctuations of the cosmic microwave background (CMB) in the line of sight of M33 is comparable to the size of the galaxy itself (see Fig. B.1). For this reason, the contribution of the CMB to the flux of M33 must be removed in a pixel-by-pixel basis instead of simply assuming an homogeneous background.

Four different CMB maps obtained with different component separation techniques are available in the *Planck* Legacy Archive (see Tab. 1 in Planck Collaboration et al. 2014e). The Spectral Matching Independent Component Analysis method (SMICA), reconstructs the CMB map as a linear combination of all the nine *Planck* frequency channels harmonically transformed up to

⁷ <http://irsa.ipac.caltech.edu/data/SPITZER/docs/mips/mipsinstrumenthandbook/>

⁸ http://herschel.esac.esa.int/Docs/PACS/html/pacs_om.html

⁹ http://herschel.esac.esa.int/Docs/SPIRE/html/spire_om.html

a multipole $\ell=4000$ (see Appendix D in Planck Collaboration et al. 2014e, for details).

Ade et al. (2014) used the SMICA map to subtract the CMB from M31, as from a visual inspection this appears to be the cleanest map of the CMB in that region from the four methods. Following these authors, we also made use of the SMICA map to remove the CMB in the line of sight of M33. The Gnomonic projection of the SMICA map was generated using the same method explained in Sect. 2.7.

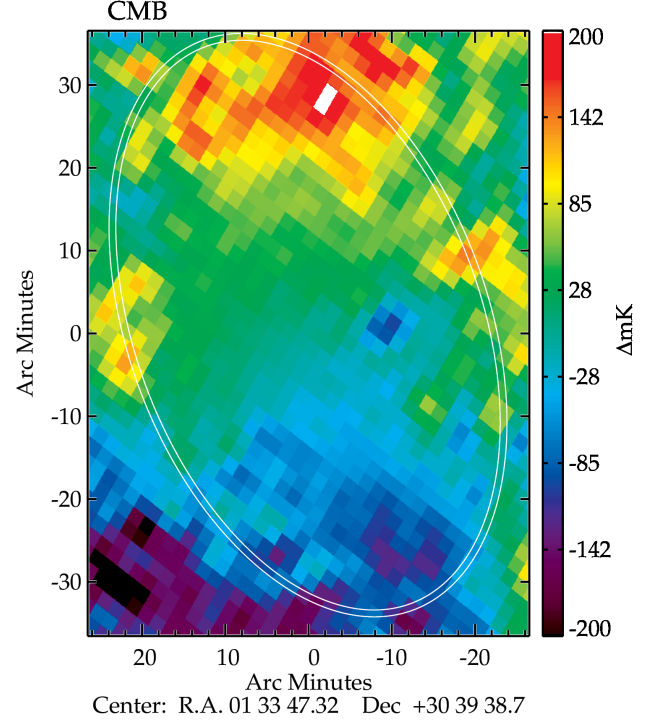


Fig. B.1: Gnomonic projection of the CMB map of *Planck* in the line of sight of M33 generated with the SMICA method. The white annulus used to subtract the local background in Fig. 1 was included here for reference. The pixel size is $2''.6$.

Appendix C: Alternative thresholds

In addition to the threshold of 40 times the background noise used in this paper to separate the SF and the diffuse components (see Sect. 3.1 for details), we also examined the results we obtain when adopting thresholds of 20 (see Fig. C.1) and 60 (see Fig. C.2). As Tab. C.1 and Tab. C.2 show, the results derived from our modeling does not depend significantly on the value of the threshold used, i.e., independently of the threshold we found i) similar deviations between the models and the observations, ii) similar dust masses, and iii) similar fractions of UV radiation escaping M33. The main reason is that the emission from the SF component constitutes only a small fraction of the total SED for most wavelengths ($100\mu\text{m} \lesssim \lambda \lesssim 1\text{ mm}$).

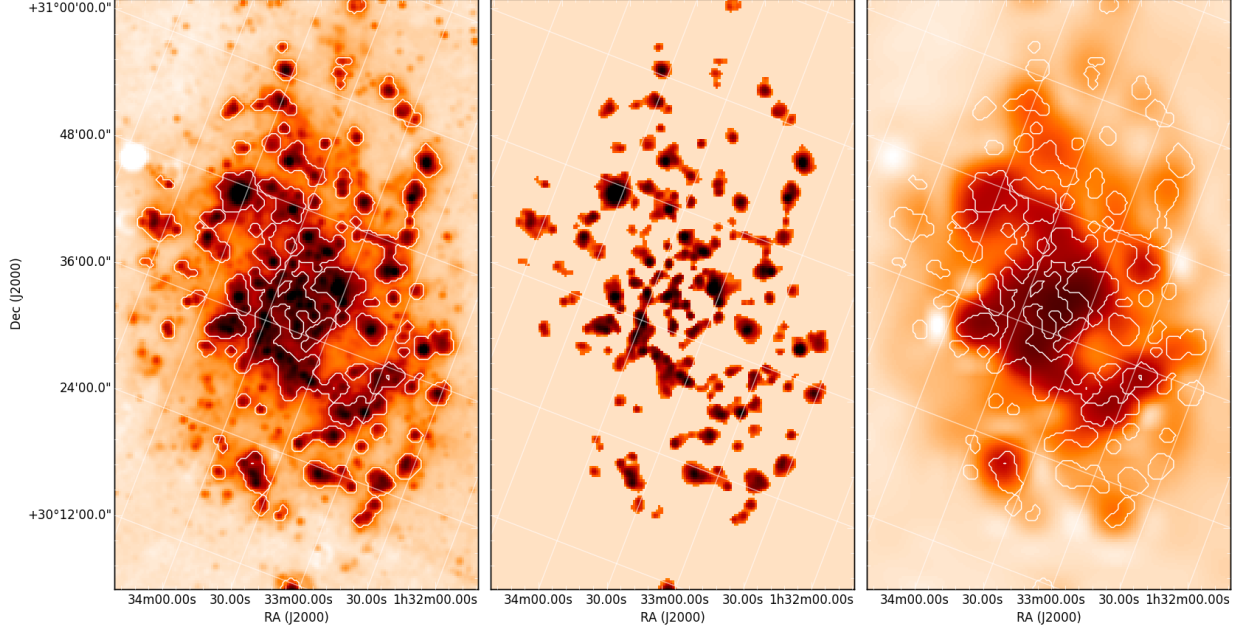


Fig. C.1: Same as Fig. 2 for a threshold of 20 times the background noise.

BAND	$\frac{S_{SF}^{obs}}{S_{SF}^{mod}}$	$\frac{\Delta_{SF}}{\sqrt{(\delta_{SF}^{obs})^2 + (\delta_{SF}^{mod})^2}}$	$\frac{S_{DIFF}^{obs}}{S_{DIFF}^{mod}}$	$\frac{\Delta_{DIFF}}{\sqrt{(\delta_{DIFF}^{obs})^2 + (\delta_{DIFF}^{mod})^2}}$	$\frac{S_{TOT}^{obs}}{S_{TOT}^{mod}}$	$\frac{\Delta_{TOT}}{\sqrt{(\delta_{TOT}^{obs})^2 + (\delta_{TOT}^{mod})^2}}$
<i>GALEX</i> FUV	-	-	-	-	$5.70^{+190.39}_{-3.01}$	5.22
<i>GALEX</i> NUV	-	-	-	-	$4.30^{+7.85}_{-3.02}$	7.49
<i>Sloan</i> <i>u</i> -band	-	-	-	-	$1.70^{+2.31}_{-1.35}$	2.68
MIPS 24 μ m	$1.15^{+1.33}_{-0.95}$	0.69	$1.01^{+1.21}_{-0.83}$	0.02	$1.04^{+1.23}_{-0.86}$	0.25
PACS 70 μ m	$0.95^{+1.05}_{-0.87}$	-0.32	$1.06^{+1.38}_{-0.83}$	0.20	$1.02^{+1.23}_{-0.85}$	0.11
PACS 100 μ m	$0.95^{+1.10}_{-0.84}$	-0.26	$0.98^{+1.17}_{-0.80}$	-0.11	$0.97^{+1.15}_{-0.81}$	-0.15
PACS 160 μ m	$0.98^{+1.15}_{-0.86}$	-0.06	$0.98^{+1.06}_{-0.85}$	-0.11	$0.98^{+1.08}_{-0.86}$	-0.09
SPIRE 250 μ m	$1.00^{+1.17}_{-0.87}$	-0.01	$0.89^{+0.97}_{-0.81}$	-0.93	$0.91^{+1.01}_{-0.82}$	-0.76
PLANCK 350 μ m	-	-	$1.02^{+1.16}_{-0.90}$	0.11	$1.02^{+1.16}_{-0.89}$	0.10
SPIRE 350 μ m	$1.10^{+1.30}_{-0.96}$	0.63	$1.03^{+1.17}_{-0.90}$	0.17	$1.03^{+1.18}_{-0.91}$	0.23
SPIRE 500 μ m	$1.29^{+1.56}_{-1.12}$	1.76	$1.14^{+1.33}_{-0.98}$	0.75	$1.17^{+1.37}_{-1.00}$	1.07
PLANCK 550 μ m	-	-	$1.36^{+1.58}_{-1.15}$	1.71	$1.31^{+1.53}_{-1.12}$	1.50
PLANCK 850 μ m	-	-	$1.62^{+1.92}_{-1.36}$	2.95	$1.54^{+1.84}_{-1.30}$	2.66
LABOCA 870 μ m	$1.80^{+2.21}_{-1.58}$	4.39	-	-	-	-
PLANCK 1.4 mm	-	-	$2.11^{+2.52}_{-1.74}$	4.83	$1.95^{+2.33}_{-1.63}$	4.38
PLANCK 2.1 mm	-	-	$1.99^{+2.39}_{-1.63}$	3.83	$1.75^{+2.08}_{-1.47}$	3.21
PLANCK 3.0 mm	-	-	$2.93^{+3.53}_{-2.40}$	7.88	$1.99^{+2.36}_{-1.68}$	4.73
PLANCK 10 mm	-	-	-	-	$0.85^{+1.00}_{-0.73}$	-0.57
S 36 mm	$0.79^{+0.94}_{-0.69}$	-1.05	-	-	$0.79^{+0.94}_{-0.69}$	-1.05

Table C.1: Same as Tab. 2 for a threshold of 20 times the background noise.

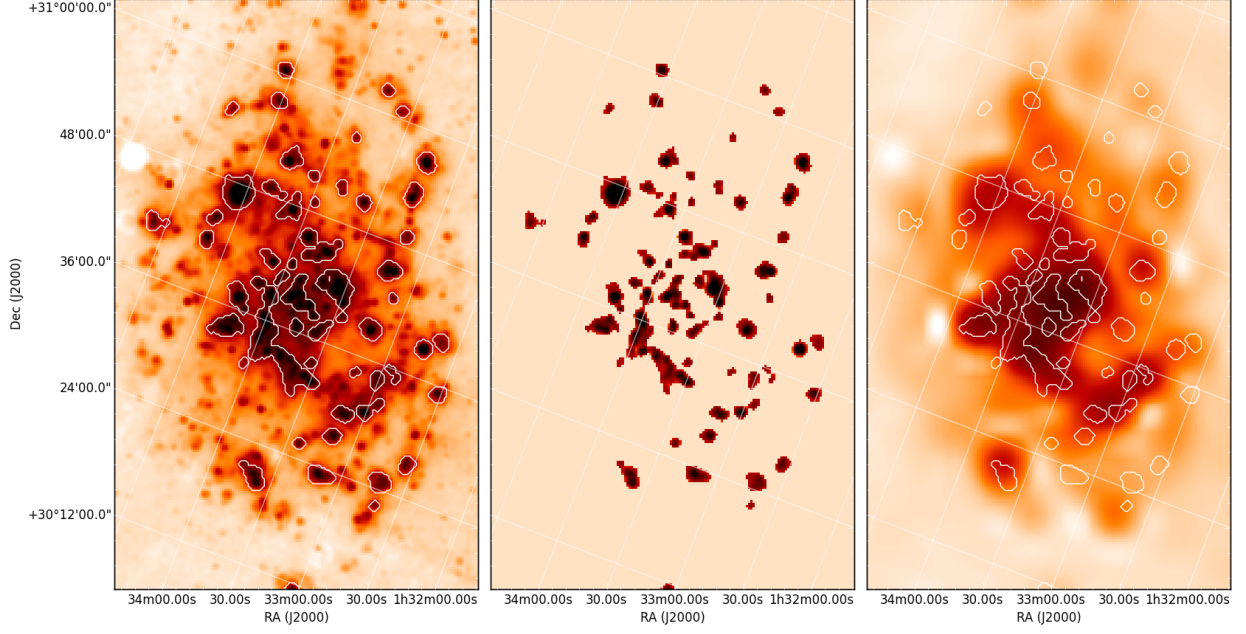


Fig. C.2: Same as Fig. 2 for a threshold of 60 times the background noise.

BAND	$\frac{S_{SF}^{obs}}{S_{SF}^{mod}}$	$\frac{\Delta_{SF}}{\sqrt{(\delta_{SF}^{obs})^2 + (\delta_{SF}^{mod})^2}}$	$\frac{S_{DIFF}^{obs}}{S_{DIFF}^{mod}}$	$\frac{\Delta_{DIFF}}{\sqrt{(\delta_{DIFF}^{obs})^2 + (\delta_{DIFF}^{mod})^2}}$	$\frac{S_{TOT}^{obs}}{S_{TOT}^{mod}}$	$\frac{\Delta_{TOT}}{\sqrt{(\delta_{TOT}^{obs})^2 + (\delta_{TOT}^{mod})^2}}$
<i>GALEX</i> FUV	-	-	-	-	$3.54^{+197.88}_{-2.40}$	5.19
<i>GALEX</i> NUV	-	-	-	-	$3.67^{+8.18}_{-2.78}$	7.81
<i>Sloan</i> u-band	-	-	-	-	$1.64^{+2.35}_{-1.33}$	2.66
MIPS 24 μ m	$1.08^{+1.25}_{-0.90}$	0.37	$1.02^{+1.29}_{-0.89}$	0.13	$1.02^{+1.24}_{-0.87}$	0.09
PACS 70 μ m	$0.99^{+1.12}_{-0.88}$	-0.03	$1.08^{+1.52}_{-0.91}$	0.36	$1.06^{+1.36}_{-0.91}$	0.23
PACS 100 μ m	$1.02^{+1.17}_{-0.88}$	0.09	$0.97^{+1.22}_{-0.84}$	-0.13	$0.98^{+1.21}_{-0.85}$	-0.09
PACS 160 μ m	$1.03^{+1.18}_{-0.90}$	0.11	$0.96^{+1.08}_{-0.86}$	-0.15	$0.98^{+1.09}_{-0.87}$	-0.10
SPIRE 250 μ m	$0.98^{+1.14}_{-0.85}$	-0.10	$0.88^{+1.04}_{-0.81}$	-0.69	$0.90^{+1.05}_{-0.82}$	-0.62
PLANCK 350 μ m	-	-	$1.01^{+1.21}_{-0.93}$	0.05	$1.01^{+1.21}_{-0.92}$	0.03
SPIRE 350 μ m	$1.06^{+1.28}_{-0.91}$	0.36	$1.02^{+1.24}_{-0.95}$	0.20	$1.02^{+1.23}_{-0.94}$	0.11
SPIRE 500 μ m	$1.21^{+1.49}_{-1.04}$	1.19	$1.14^{+1.40}_{-1.03}$	1.05	$1.15^{+1.42}_{-1.04}$	1.20
PLANCK 550 μ m	-	-	$1.32^{+1.63}_{-1.19}$	2.03	$1.29^{+1.59}_{-1.16}$	1.80
PLANCK 850 μ m	-	-	$1.57^{+1.97}_{-1.39}$	3.77	$1.52^{+1.90}_{-1.34}$	3.39
LABOCA 870 μ m	$1.72^{+2.14}_{-1.48}$	3.62	-	-	-	-
PLANCK 1.4 mm	-	-	$2.04^{+2.57}_{-1.78}$	6.02	$1.92^{+2.42}_{-1.68}$	5.38
PLANCK 2.1 mm	-	-	$1.93^{+2.46}_{-1.68}$	4.56	$1.75^{+2.18}_{-1.51}$	3.57
PLANCK 3.0 mm	-	-	$2.86^{+3.64}_{-2.47}$	9.90	$2.02^{+2.51}_{-1.71}$	5.01
PLANCK 10 mm	-	-	-	-	$0.89^{+1.09}_{-0.74}$	-0.38
S 36 mm	$0.84^{+1.02}_{-0.69}$	-0.75	-	-	$0.84^{+1.02}_{-0.69}$	-0.75

Table C.2: Same as Tab. 2 for a threshold of 60 times the background noise.